Worlds Next Door: A Candidate Giant Planet Imaged in the Habitable Zone of α Centauri A. II. Binary Star Modeling, Planet and Exozodi Search, and Sensitivity Analysis

Aniket Sanghi, Charles Beichman, Dimitri Mawet, William O Balmer, Nicolas Godoy, Laurent Pueyo, Anthony Boccaletti, Max Sommer, Alexis Bidot, Elodie Choquet, et al.

The Astrophysical Journal Letters, 989:L23 (24pp), 2025 August 20 https://doi.org/10.3847/2041-8213/adf53e

Worlds Next Door: A Candidate Giant Planet Imaged in the Habitable Zone of α Centauri A. II. Binary Star Modeling, Planet and Exozodi Search, and Sensitivity Analysis

Aniket Sanghi[1,2,13], Charles Beichman[3,4,13], Dimitri Mawet[1,4], William O. Balmer[5,6], Nicolas Godoy[7], Laurent Pueyo[6], Anthony Boccaletti[8], Max Sommer[9], Alexis Bidot[6], Elodie Choquet[7], Pierre Kervella[8,10], Pierre-Olivier Lagage[11], Jarron Leisenring[12], Jorge Llop-Sayson[4], Michael Ressler[4], Kevin Wagner[12], and Mark Wyatt[9]

[1] Cahill Center for Astronomy and Astrophysics, California Institute of Technology, 1200 East California Boulevard, MC 249-17, Pasadena, CA 91125, USA; asanghi@caltech.edu
[2] NSF Graduate Research Fellow
[3] NASA Exoplanet Science Institute, Caltech-IPAC, Pasadena, CA 91125, USA; chas@ipac.caltech.edu
[4] Jet Propulsion Laboratory, California Institute of Technology, Pasadena, CA 91109, USA
[5] Department of Physics & Astronomy, Johns Hopkins University, 3400 North Charles Street, Baltimore, MD 21218, USA
[6] Space Telescope Science Institute, 3700 San Martin Drive, Baltimore, MD 21218, USA
[7] Aix Marseille Université, CNRS, CNES, LAM, Marseille, France
[8] LIRA, Observatoire de Paris, Université PSL, Sorbonne Université, Université Paris Cité, CY Cergy Paris Université, CNRS, 5 Place Jules Janssen, 92195 Meudon, France
[9] Institute of Astronomy, University of Cambridge, Madingley Road, Cambridge CB3 0HA, UK
[10] French-Chilean Laboratory for Astronomy, IRL 3386, CNRS and Universidad de Chile, Casilla 36-D, Santiago, Chile
[11] Université Paris-Saclay, Université Paris Cité, CEA, CNRS, AIM, 91191 Gif-sur-Yvette, France
[12] Steward Observatory, University of Arizona, Tucson, AZ 85721, USA
Received 2025 June 26; revised 2025 July 25; accepted 2025 July 28; published 2025 August 11

Abstract

The James Webb Space Telescope (JWST) observed our closest solar twin, α Centauri A (α Cen A), with the Mid-Infrared Instrument in the F1550C (15.5 μm) coronagraphic imaging mode at three distinct epochs between 2024 August and 2025 April. For the first time with JWST, we demonstrate the application of reference star differential imaging to simultaneously subtract the coronagraphic image of a primary star (α Cen A) and the point-spread function (PSF) of its binary companion (α Cen B) to conduct a deep search for exoplanets and exozodiacal dust emission. We achieve a typical 5σ point-source contrast sensitivity between $\sim 10^{-5}$ and 10^{-4} at separations $\gtrsim 1''$ and an exozodiacal disk (coplanar with α Cen AB) sensitivity of $\sim$5–8$\times$ the solar system's zodiacal cloud around α Cen A. The latter is an extraordinary limit, representing the deepest sensitivity to exozodiacal disks achieved for any stellar system to date. Additionally, postprocessing with the principal-component-analysis-based Karhunen–Loéve image processing algorithm reveals a point source, called *S*1, in 2024 August, detected at signal-to-noise ratio of 4–6 (3.3–4.3σ), a projected separation of $\approx 1\farcs5$ (2 au), and with an F1550C flux density (contrast) of $\approx$3.5 mJy ($\approx 5.5 \times 10^{-5}$). Various tests conducted with the available data show that *S*1 is unlikely to be a detector artifact or PSF-subtraction artifact and confirm that it is neither a background nor a foreground object. *S*1 is not redetected in two follow-up observations (2025 February and April). If *S*1 is astrophysical in nature, the only explanation is that it has moved to a region of poor sensitivity due to orbital motion. We perform PSF injection–recovery tests and provide 2D sensitivity maps for each epoch to enable orbital completeness calculations. Additional observations, with JWST or upcoming facilities, are necessary to redetect candidate *S*1 and confirm its nature as a planet orbiting our nearest solar-type neighbor, α Cen A. More broadly, this program highlights the complexity of analyzing a dynamic binary astrophysical scene and the challenges associated with confirming short-period ($\sim$few years) planet candidates identified without prior orbital constraints in direct imaging searches. This Letter is second in a series of two papers: Paper I discusses the observation strategy and presents the astrophysical case (physical and orbital properties) for *S*1 as a planet candidate.

Unified Astronomy Thesaurus concepts: James Webb Space Telescope (2291); Coronagraphic imaging (313); Extrasolar gaseous giant planets (509); Exozodiacal dust (500)

1. Introduction

At a distance of 1.34 pc from Earth, α Centauri (α Cen) is the solar system's nearest known neighbor. This stellar system has three components in a hierarchical orbital configuration: α Cen A (Rigil Kentaurus) and α Cen B (Toliman) together form an eccentric close binary (semimajor axis = 23.3 au, $e = 0.52$; R. Akeson et al. 2021) and are orbited by Proxima Centauri (α Cen C) at a distance of $\approx$8200 au. The α Cen system's age is estimated to be 5.3 ± 0.3 Gyr (F. Thévenin et al. 2002; M. Joyce

[13] Shared first authorship.

& B. Chaboyer 2018), similar to our solar system's age of ∼4.6 Gyr. Among the three components, α Cen A (G2V, $M_A = 1.0788\,M_\odot$, $R_A = 1.2175\,R_\odot$; R. Akeson et al. 2021) stands out as the closest Sun-like star to Earth and is an exceptional target for exoplanet direct imaging searches. It is ≈2.7 times closer and ≈3.3 times more luminous than the next most favorable G-type star τ Ceti. This places the habitable zone of α Cen A (defined as the separation of Earth-equivalent insolation, ≈1.27 au; M. C. Turnbull 2015) at a modest angular separation of 0.″95 (compared to 0.″2 for τ Ceti), resolvable by current ground- and space-based telescopes.

Presently, there are no confirmed planets around α Cen A. While α Cen B could be responsible for removing planets from the system, dynamical studies suggest a stable zone exists at separations $\lesssim 3$ au around α Cen A where planets could survive over long timescales (P. A. Wiegert & M. J. Holman 1997; B. Quarles & J. J. Lissauer 2016). The earliest attempts to image companions around α Cen A used the Hubble Space Telescope's Planetary Camera in the near-infrared at 1.02 μm (D. J. Schroeder & D. A. Golimowski 1996; D. J. Schroeder et al. 2000). These observations were sensitive to 5 Gyr old brown dwarfs with masses $> 40\,M_{\rm Jup}$ at separations $> 5''$ from α Cen A. More recently, a 100 hr high-contrast imaging (HCI) campaign with the VISIR mid-infrared camera (10–12.5 μm) on ESO's Very Large Telescope (VLT) as part of the New Earths in Alpha Centauri Region (NEAR) Breakthrough Watch Project detected a candidate object, called *C*1, at a separation of ≈1.1 au (K. Wagner et al. 2021). The source could be a $\gtrsim$300 K planet with a radius $\gtrsim 3.3\,R_\oplus$ or dust in a ∼60 Zodi disk. It has not been possible to reobserve *C*1 to confirm its nature and exclude alternate possibilities such as an instrumental artifact of unknown origin. Additionally, precision radial velocity measurements limit the minimum mass, $M\sin(i)$, of any planet orbiting α Cen A with a period $\lesssim$ 1000 days to be $\lesssim 100\,M_\oplus$ ("red noise" simulations; L. Zhao et al. 2018).

The launch of the James Webb Space Telescope (JWST) opens up new avenues for direct imaging planet and disk searches around α Cen A (C. Beichman et al. 2020; A. Sanghi et al. 2025). Preflight simulations by C. Beichman et al. (2020) showed that the JWST Mid-Infrared Instrument (MIRI) coronagraph (A. Boccaletti et al. 2015; G. S. Wright et al. 2015) at 15.5 μm can image planets as small as 5 $R_\oplus$ at separations of 1–3 au including, potentially, the VLT/NEAR *C*1 candidate. Additionally, with its ability to resolve α Cen A's habitable zone, JWST/MIRI could also detect an exozodiacal dust cloud only ∼3–5× the brightness of the solar system's zodiacal cloud (C. Beichman et al. 2020). In this Letter, we present results from three epochs of JWST/MIRI coronagraphic imaging observations of α Cen A, conducted as part of a deep search for planets and zodiacal dust emission in α Cen A's habitable zone. This Letter is the second in a series and is preceded by C. Beichman et al. (2025; hereafter Paper I). It is organized as follows. Section 2 summarizes the observational sequences executed with JWST. Section 3 discusses the initial preprocessing steps for the data. Section 4 describes the stellar point-spread function (PSF) modeling and subtraction procedures with the first epoch observations and investigates the nature of a candidate planetary signal. Section 5 presents the results after PSF subtraction for the second and third epoch observations and discusses if the candidate is recovered either as a background object or an orbiting companion. Section 6 details the procedures used to estimate the astrometry and photometry of the candidate. Section 7 presents the overall sensitivity of our observations to planets around α Cen A. Section 8 discusses our search for extended emission and places new upper limits on its presence around α Cen A. Finally, Section 9 summarizes our conclusions. Appendix A demonstrates the benefits of using all reference integrations without binning in PSF subtraction and Appendix B presents the recovery of a known, faint, background source in the individual epoch data sets.

2. Summary of Observations

Here, we provide a summary of JWST observations of the nearest solar-type star, α Cen A. For a complete description, we refer the reader to Paper I. JWST successfully observed α Cen A through the MIRI coronagraph in the F1550C (15.5 μm) filter on three separate occasions: 2024 August (Cycle 1 GO, PID #1618; PI: Beichman, Co-PI: Mawet), 2025 February (Cycle 3 Director's Discretionary Time (DDT), PID #6797; PI: Beichman, Co-PI: Sanghi), and 2025 April (Cycle 3 DDT, PID #9252; PI: Beichman, Co-PI: Sanghi). The observing setup and strategy were identical for all three observation epochs.

2.1. Executed Sequences

The observations were designed to acquire two roll angle sequences of α Cen A to improve sensitivity with reference star differential imaging (RDI; D. Lafrenière et al. 2009) by (1) providing a means to de-correlate diffraction features from α Cen A and α Cen B, and (2) modulating the transmission of the coronagraph in case a source falls near the coronagraph transition boundary for one of the rolls. It also enables angular differential imaging (ADI; M. C. Liu 2004; C. Marois et al. 2006), however, significant gains compared to RDI are not expected at small angular separations (e.g., A. L. Carter et al. 2023). The total duration of the exposure per roll angle was 9287.36 s comprising of 1250 integrations. However, due to guide star failures, only one roll angle observation was obtained both in 2024 August and 2025 February. A full two roll angle sequence (9° roll) was obtained in 2025 April.

The reference star for these observations, ϵ Mus, was observed twice, bracketing the two roll angle observations of α Cen A, with the MIRI coronagraph (F1550C) in a nine-point small grid dither (SGD) pattern. This enables us to assemble a coronagraphic image library with a diversity of stellar positions behind the Four Quadrant Phase Mask (4QPM) for RDI and maximize the chance of obtaining a well-matched PSF reference for α Cen A. The total duration of the exposure, per dither position, was 2971.792 s comprising of 400 integrations. One of the SGD sequences in 2024 August suffered from a guide star failure. Both SGD sequences were successful in 2025 February and April.

We also placed the reference star, ϵ Mus, at the off-axis position of α Cen B on the MIRI detector and observed it with the coronagraph in the optical path (F1550C). This enables us to obtain accurate reference images for the removal of α Cen B's PSF in postprocessing.[14] Note that the detector

[14] α Cen A was also observed in 2024 July to test the offset strategy for target acquisition. However, no ϵ Mus reference at the detector position of α Cen B was acquired. Hence, this data set was not found to be suitable for a planet or exozodi search.

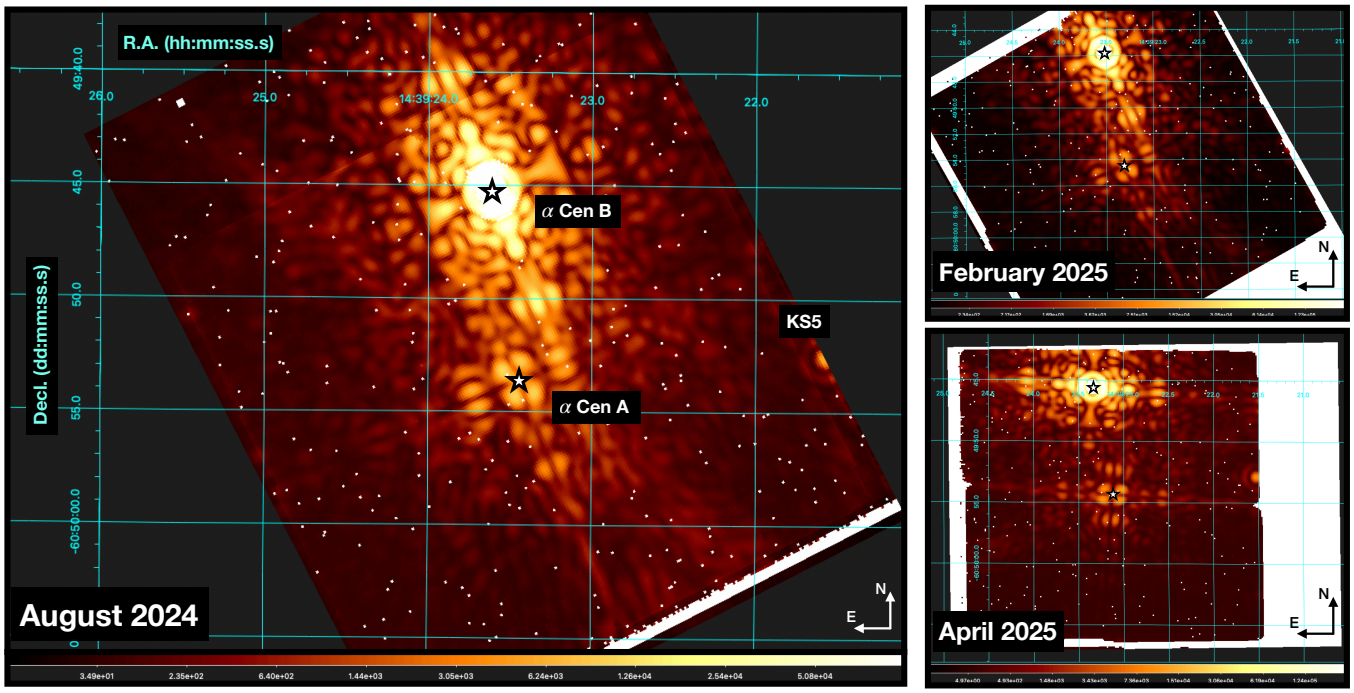

Figure 1. Left: an "off-the-shelf" Stage 2b F1550C image of the α Cen AB system downloaded from the Mikulski Archive for Space Telescopes (MAST) for the 2024 August observation (no bad-pixel correction). The image is oriented north up and east left. The white stars denote the approximate positions of α Cen B, saturated near the top of the image, and α Cen A in the lower part of the image placed behind the 4QPM. At the edge of the detector, to the west of α Cen A, is a known background source, KS5 (P. Kervella et al. 2016). The color bar is logarithmically scaled in units of MJy sr^{-1}. Right: same as the left image for 2025 February (top) and 2025 April (bottom).

position of α Cen B changes between observations at the two roll angles. Thus, two distinct off-axis ϵ Mus reference observations were required. The total duration of the exposure per observation was 9287.36 s comprising of 1250 integrations. All planned off-axis ϵ Mus reference observations were successful across the three observation dates.

Finally, to mitigate the effects of the MIRI "glowstick" (A. Boccaletti et al. 2022), we obtained dedicated backgrounds for each science observation (matching detector setups). The position of the background observation was chosen such that it appeared relatively blank in Spitzer Space Telescope or Wide-field Infrared Survey Explorer images. Background images were acquired immediately after each α Cen roll and ϵ Mus on-axis reference observation (the off-axis ϵ Mus observations have the same detector setup as the α Cen rolls and the corresponding background images are reused). Each background field was observed twice (for a given observation) with 5″ shifts in the center position to help mitigate the effects of sources in the fields.

2.2. An Unusual High-contrast Imaging Astrophysical Scene

The α Cen AB system is a complex and dynamic astrophysical scene (Figure 1), distinct from those tackled by traditional direct imaging programs, which is both challenging for MIRI observations (as discussed in Paper I) and data analysis. First, the position of α Cen A behind the MIRI 4QPM is inconsistent between observation epochs (and even between two rolls acquired in the same epoch) at the ∼10 mas level (Section 3.2) because of uncertainties in the blind offset target acquisition procedure (see Paper I). This changes the coronagraphic image of α Cen A for every observation. Second, a deep search for planets and exozodiacal emission not only requires the subtraction of residual starlight from α Cen A behind the MIRI coronagraph, but also from its binary companion. α Cen B is observed ∼7″–8″ away at full brightness on the MIRI detector, unocculted, and with its PSF diffraction features superimposed on those from α Cen A's coronagraphic image in the region of interest for planet and disk searches. Third, α Cen B's position on the detector and PSF orientation both change for every observation epoch (Figure 1) due to orbital motion and the exact V3 position angle (PA) of observation,[15] respectively. This, for example, restricts us to only using reference frames acquired in the same epoch for postprocessing and affects the achieved sensitivity (as discussed in Section 7). Thus, α Cen AB is a unique system for HCI data reduction. In this Letter, we develop novel techniques to analyze such data sets.

3. Data Preprocessing

3.1. JWST Pipeline Processing

We obtained the raw (*uncal.fits) images from MAST. The images were preprocessed using `spaceKLIP` (J. Kammerer et al. 2022; A. L. Carter et al. 2023; A. Carter et al. 2025), a community-developed repository that wraps key `jwst` (H. Bushouse et al. 2025) pipeline steps with modifications and additions appropriate for HCI. The reduction used the `jwst` pipeline version 1.18.0, the Calibration Reference Data System (CRDS) version 12.1.7, and the CRDS context file `jwst_1364.pmap`. We skipped dark current subtraction, to avoid introducing additional noise due to the low signal-to-noise ratio (S/N) of the available darks. The data were read "up the ramp" using the `LIKELY` algorithm described in

[15] V3PA is the position angle (PA) of the V3 reference axis eastward relative to north when projected onto the sky.

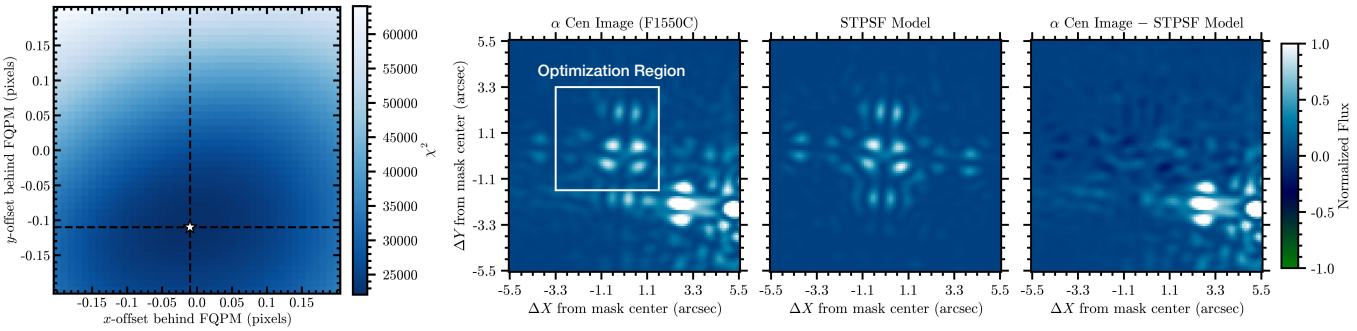

Figure 2. Example determination of stellar position behind the MIRI 4QPM for α Cen A in the 2024 August observation. Left: χ^2 map obtained after subtracting `STPSF` models generated by varying the stellar position behind the mask (marginalized over the model PSF flux scale factor parameter). The best-fitting PSF (minimum χ^2) is marked with a white star. Right: from left to right, the observed α Cen A PSF, best-fitting `STPSF` model, and residual image after taking the difference are shown. The white box designates the region over which χ^2 was minimized.

T. D. Brandt (2024) and corrected for jumps using a threshold of eight (following previous work with MIRI coronagraphy; A. Boccaletti et al. 2022; A. L. Carter et al. 2023; M. Mâlin et al. 2024). We skipped the flat-fielding Stage 2 calibration step, to avoid biasing photometry of sources near the transitions of the 4QPM following M. Mâlin et al. (2024, 2025).

The Stage 2 (*calints.fits) images were iteratively corrected for bad pixels (cosmic rays, hot pixels, dead pixels, etc). First, pixels flagged during the ramp fitting stage, and by the `jwst` pipeline during Stage 2, were filled in with an interpolating spline with a kernel size of 3 pixels. Then, temporal outliers (between integrations in a given pointing) were flagged using sigma clipping with a threshold of six, and replaced with their temporal median. Finally, additional spatial outliers were flagged using sigma clipping with a threshold of three and a search box of 5 pixels on a side, and replaced with an interpolating spline with a kernel size of 3 pixels, as in the first step. Once corrected for bad pixels, the associated MIRI 4QPM background exposures were subtracted from the α Cen AB science, ϵ Mus on-axis reference, and ϵ Mus off-axis reference exposures that matched their readout pattern.

3.2. Stellar Positions behind the MIRI/Four Quadrant Phase Mask

Estimating the position of ϵ Mus and α Cen A behind the MIRI/4QPM enables (1) verification of the accuracy of target acquisition with blind offsets from background stars; (2) determination of the pointing stability between observations in the nine-point SGD observation of ϵ Mus; and (3) identification of the ϵ Mus reference observation that best matches the α Cen A PSF. Broadly, we find the stellar position behind the MIRI/4QPM by minimizing the χ^2 on comparison with a grid of `STPSF` models (M. D. Perrin et al. 2012; M. D. Perrin et al. 2014) generated for varying offsets. The detailed steps are described below.

We begin with the background-subtracted Stage 2b data products obtained following the processing steps described in Section 3.1. For ϵ Mus, we average the 400 integrations at each dither position and for α Cen A, the 1250 integrations at the single roll to obtain mean frames for comparison with `STPSF` models. The uncertainty estimate for each pixel in a given integration is retrieved from the `ERR` extension in the `calints` data product and appropriately combined to obtain the per-pixel uncertainty for the mean frames. Next, we define the region over which χ^2 is optimized. For ϵ Mus, we select a 90×90 pixel subarray centered on the coronagraph center as retrieved from the `CRPIX1` and `CRPIX2` header values. For α Cen A, we select a 45×45 pixel subarray encompassing the central PSF but offset to exclude the majority of the two quadrants where there is significant contamination from the unocculted off-axis PSF of α Cen B (example in Figure 2). `STPSF` models are computed for a grid of pointing offsets between -0.2 and 0.2 pixels (-22 mas to 22 mas) in steps of 0.01 pixels (1.1 mas) along each axis. The models include detector effects (interpixel capacitance and charge diffusion),[16] are generated using the closest-in-time on-sky optical path difference (OPD) map to the observations, and oversampled by a factor of 4.

The fitting procedure registers the `STPSF` model to the mean comparison frame using a Fourier image shift (A. Z. Greenbaum et al. 2023) implemented with the `webbpsf_ext` package (J. Leisenring 2025). The required shift is determined with the `image_registration` package's `chi2_shift` function and is applied to the oversampled model PSF before binning down to the native detector sampling. We compute χ^2 over all pixels in the optimization region for the grid of stellar positions behind the mask as well as a varying flux scale factor for the model PSFs. A noise floor was applied to the pixels in the optimization regions to ensure that the pixels belonging to the image background do not artificially inflate the χ^2 value. We selected the smallest uncertainty value among pixels that were a part of prominent features of the stellar diffraction pattern in the optimization region as the noise floor. A clear χ^2 minimum is identified for all α Cen A observations and all ϵ Mus observations (one example shown in Figure 2). The typical uncertainty in our estimate of the stellar position behind the mask is 1.1 mas.

Our estimates of the stellar position behind the mask for the ϵ Mus and α Cen A observations indicate that the initial coronagraph pointing after blind offsets is accurate to $\sim$10 mas along each axis (Figure 3), consistent with the typical pointing accuracy of MIRI coronagraphic observations (A. Boccaletti et al. 2022; J. Rigby et al. 2023). The nine-point SGD pattern was effective at providing a reference PSF that closely matches the 2024 August science observation (Figure 3). However, due to a significant pointing mismatch ($\approx$25 mas between α Cen A and the SGD center), none of the

[16] https://stpsf.readthedocs.io/en/latest/jwst_detector_effects.html

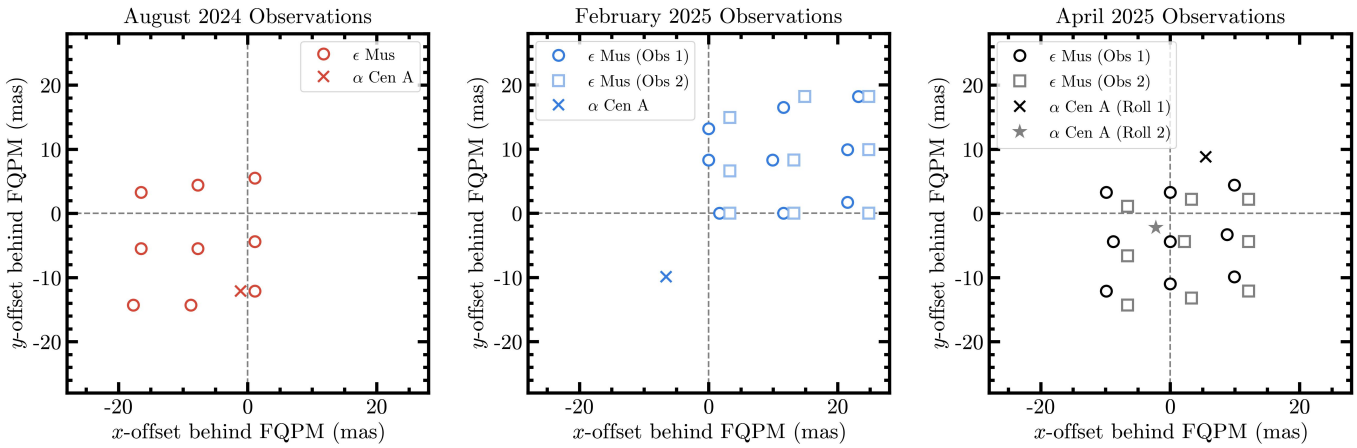

Figure 3. Estimated positions of ϵ Mus and α Cen A behind the MIRI/4QPM in the nine-point SGD and single/two roll observations, respectively, for each observation epoch (with respect to mask center). The 2024 August and 2025 April (roll 2 only) α Cen A observations have ϵ Mus reference images well matched in terms of position behind the 4QPM.

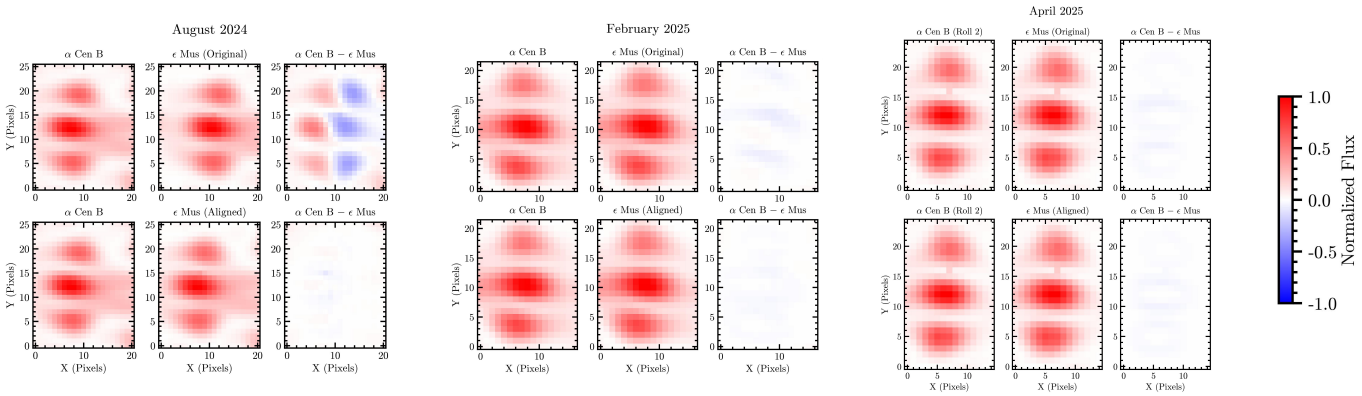

Figure 4. Alignment of the off-axis ϵ Mus reference frames to the corresponding α Cen B observations using a bright diffraction feature in each of the epochs (for 2025 April, only the roll 2 observation is shown). Top panel: for a given epoch, from left to right, the α Cen B observation, ϵ Mus reference frame, and difference image. Bottom panel: similar to the top panel but with the ϵ Mus reference frame aligned to the α Cen B observation.

dithered reference positions closely match that of the 2025 February science observation. For the 2025 April science observations, the SGD was effective at providing reference PSFs bracketing the position of α Cen A behind the 4QPM for roll 2, but not for roll 1.

3.3. Off-axis ϵ Mus Reference Image Alignment

The off-axis ϵ Mus observations serve as a reference for the subtraction of α Cen B's PSF. First, we need to align the off-axis ϵ Mus reference frames to their corresponding science observation for each observation epoch. The images are registered over a small subarray centered on a bright α Cen B diffraction feature using an interpolation-based image shift implemented with the `pyklip.klip.align_and_scale` function (J. J. Wang et al. 2015). We did not use Fourier image shifts as they introduced Gibbs artifacts in the shifted images from the saturated regions of α Cen B's PSF. The diffraction feature was chosen such that it avoids saturated regions of the α Cen B PSF and shows a structure distinct from α Cen A's features. The required shift is determined with the `image_registration` package's `chi2_shift` function (Figure 4). We find that an (x, y) shift of $(-3.00, -0.10)$ pixels is needed to align the ϵ Mus reference PSF to α Cen B's PSF in the 2024 August observations. Similarly, for the 2025 February observation we require an (x, y) shift of $(-0.10, -0.10)$ pixels. For roll 1 and 2 of the 2025 April observation, the shift required to align the associated off-axis ϵ Mus reference PSF is (0.03, 0.06) pixels and (0.03, −0.04) pixels, respectively.

4. 2024 August Data Postprocessing

In this section, our goal is to conduct a comprehensive search for point sources representing planetary companions around α Cen A, within a radial field of view $< 5''$, in the 2024 August observations. According to dynamical stability arguments (e.g., P. A. Wiegert & M. J. Holman 1997), planets could exist within approximately 4 au ($\approx 3''$) of α Cen A. We employ RDI to subtract both α Cen A and α Cen B and explore two distinct PSF-subtraction strategies to ensure robustness of any detections, as detailed below. The failure of the second roll observation of α Cen A, in 2024 August, precludes the use of ADI. The PSF-subtracted images are visually inspected for point sources. A corresponding S/N map is generated for each reduction following the definition in D. Mawet et al. (2014) using the `snrmap` function in `vip_hci` (C. A. Gomez Gonzalez et al. 2017; V. Christiaens et al. 2023) and is used to assess the strength of any candidates identified.

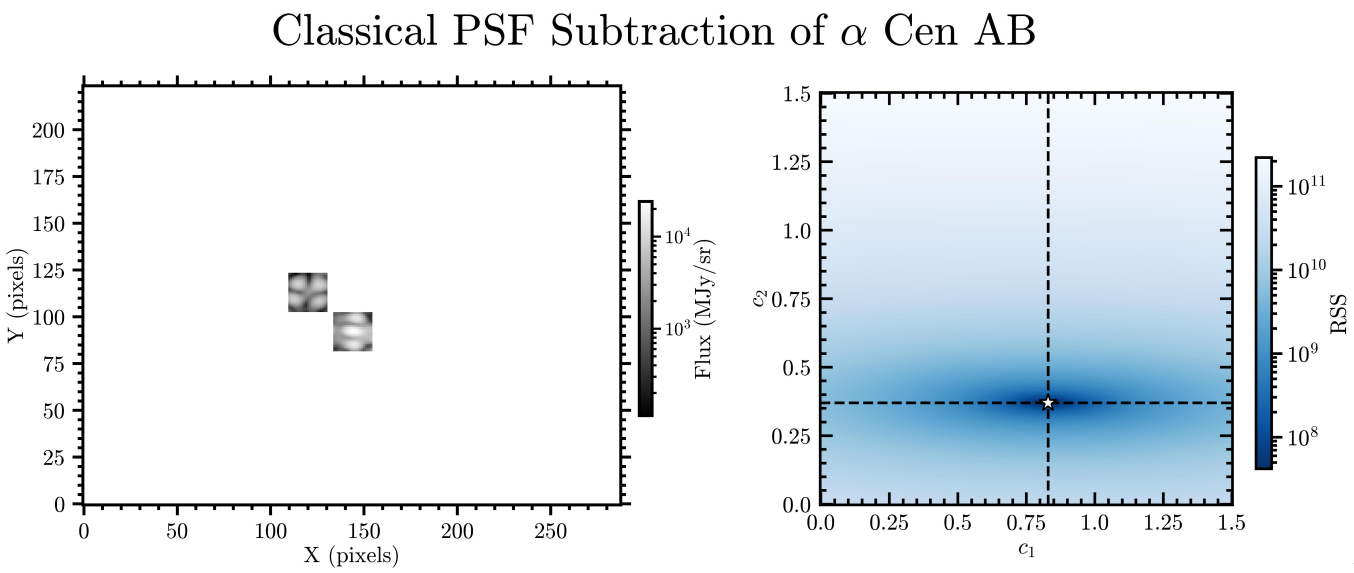

Figure 5. Subtraction of α Cen AB using a linear combination of reference images. Left: full α Cen AB detector image showing the regions over which the RSS was minimized to obtain coefficients c_1 (for α Cen A's PSF model) and c_2 (for α Cen B's PSF model). Right: RSS map obtained after subtracting the model PSFs. The best-fitting (minimum RSS) coefficient pair ($c_1 = 0.830$, $c_2 = 0.370$) is marked with a white star.

4.1. Classical Point-spread Function Subtraction: Median Reference Star Differential Imaging

The 1250 α Cen AB images are median combined to produce a single science image for the PSF-subtraction procedure. We use the median-combined seventh dither observation of ϵ Mus ($\mathrm{PSF}_{\epsilon,\ \mathrm{on}}$) as the reference model for α Cen A's PSF due to its similarity in position behind the MIRI/4QPM (see Section 3.2) and the median-combined aligned off-axis observation of ϵ Mus ($\mathrm{PSF}_{\epsilon,\ \mathrm{off}}$) as the reference model for α Cen B's PSF. The combined PSF model for α Cen AB is then constructed as the linear combination $c_1 \cdot \mathrm{PSF}_{\epsilon,\ \mathrm{on}} + c_2 \cdot \mathrm{PSF}_{\epsilon,\ \mathrm{off}}$. The optimization region for PSF subtraction is chosen to include bright diffraction features from both α Cen A and α Cen B and is visualized in Figure 5. This was inspired by the zone selection methodology of the Locally Optimized Combination of Images algorithm (D. Lafreniere et al. 2007). We find that the coefficient pair ($c_1 = 0.830$, $c_2 = 0.370$) minimizes the residual sum of squares (RSS) in the optimization region (Figure 5). We experimented with different sets of optimization regions and found similar values for c_1 and c_2. The above values are adopted for PSF subtraction below.

PSF subtraction is performed over the full detector image using the reference PSFs with the coefficients determined above and the residual image is de-rotated to align north up and east left. Two point-like sources labeled $S1$ and $A1$ are identified around α Cen A within the approximate region of dynamical stability by visual inspection (Figure 6(a)) and for $\mathrm{S/N} > 2.5$. Sources $S1$ and $A1$ are detected at a peak S/N of 3.6 and 2.8 (Figure 6(b)), respectively. $A1$ is directly associated with a bright diffraction feature of the α Cen B PSF (Figure 6(d)). $S1$ is next to a diffraction feature of the α Cen B PSF and may be associated with it (Figure 6(d)). The following, more robust and sensitive, principal component (PC) analysis Kahrunen–Loéve image processing (PCA-KLIP) analysis will help distinguish diffraction and/or speckle artifacts from true astrophysical sources. The S/N map shows additional structure in the northwest quadrant, however these lie along the axis of α Cen B's PSF.

4.2. Joint Principal Component Analysis Kahrunen–Loéve Image Processing Modeling of α Cen AB

In this approach, we model and subtract the stellar diffraction pattern from α Cen A and α Cen B using the PCA-KLIP algorithm (R. Soummer et al. 2012). We use a single reference library consisting of both the on- and off-axis ϵ Mus reference frames to construct a PSF model for a given subtraction region.[17]

4.2.1. Point-spread Function Subtraction with Automatic Principal Component Selection

We begin by conducting a blind search for astrophysical sources in the vicinity of α Cen A. We perform reductions where joint PCA-KLIP is applied to a single annulus with a radial size of 2 FWHM ($\approx 1''$) and centered at varying radial separations between $0''.75$ and $3''.5$ in steps of $0''.25$ (12 different reductions). We allow the `pca_annulus` function in `vip_hci` to automatically select the optimal number of PCs for each annulus as the value at which the standard deviation of the residuals (after the subtraction of the PCA approximation) drops below a tolerance value = 0.1. Smaller tolerance values lead to the use of a larger number of PCs. The motivation behind this method of selecting the number of PCs is to optimize the subtraction with respect to the noise while remaining agnostic to possible (a priori, unknown) signals. This strategy works well for RDI reductions, where the PCs do not depend on the astrophysical signal (oversubtraction). However, we note that this is not applicable for ADI reductions, where the PCs do depend on the astrophysical signal (self-subtraction) and optimizing on the noise rather than the signal can significantly impact detectability (L. Pueyo 2016).

After an extensive search across all our reductions, only one point source was detected at $\mathrm{S/N} > 5$. As a summary, we show a representative postprocessed image (and the corresponding

[17] We also explored sequentially subtracting α Cen B, first, followed by α Cen A, second, with PCA-KLIP. However, this proved challenging due to oversubtraction in the vicinity of α Cen A after performing the first step.

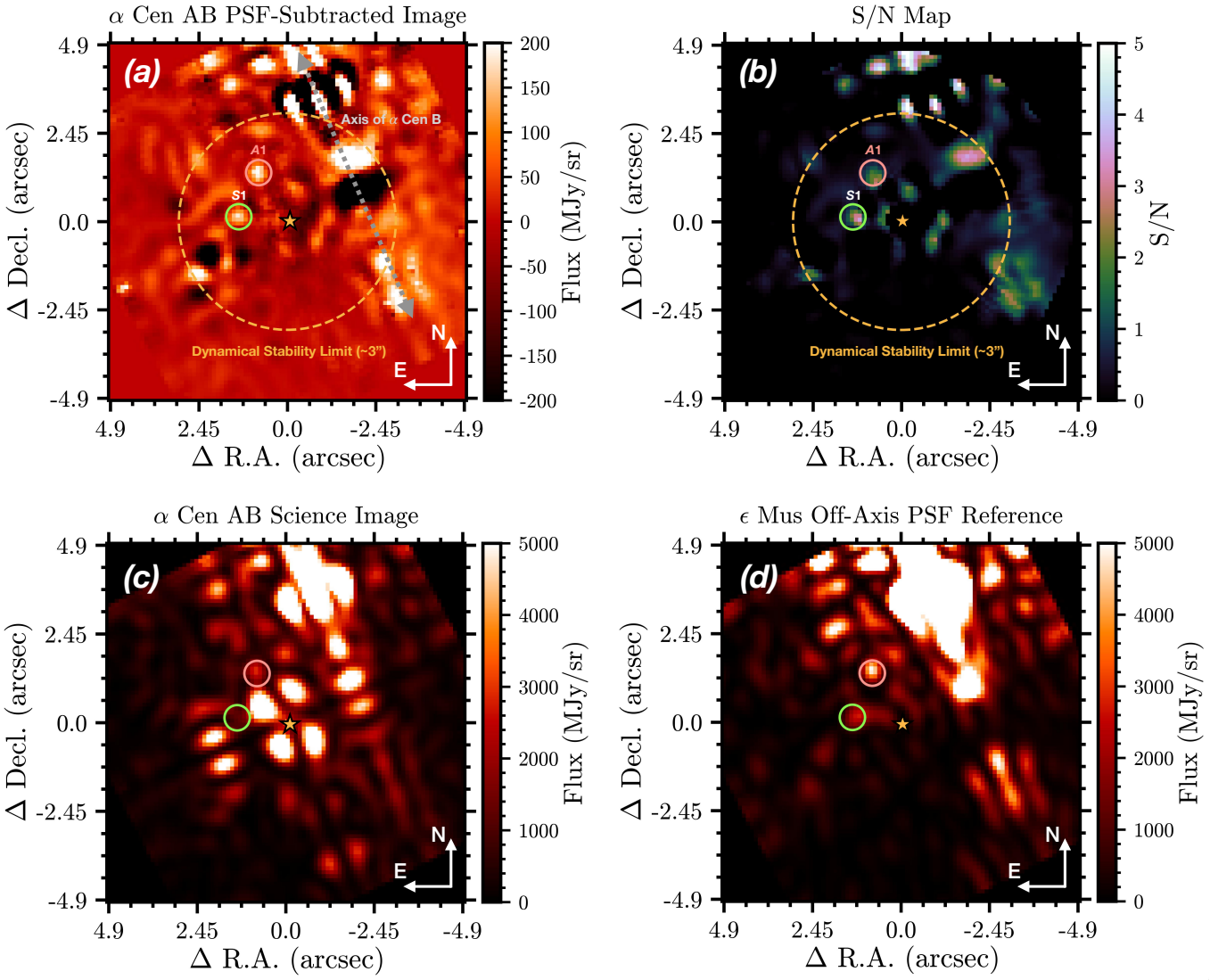

Figure 6. Results from classical PSF subtraction of α Cen AB for the 2024 August observations. Top panel: the de-rotated residual image (a; north up, east left) and associated S/N map (b) after subtraction of α Cen AB with a linear combination of reference images, using the best-fit c_1 and c_2 coefficient values. Visually identified point sources, *S*1 and *A*1, are circled. The star symbol marks the center of α Cen A. Bottom panel: the left image (c) is the de-rotated α Cen AB science integration before PSF subtraction and the right image (d) is the de-rotated off-axis ϵ Mus reference for α Cen B. The latter acts as a proxy for and shows the diffraction features expected from α Cen B in vicinity of α Cen A. A red circle marks the position of *A*1, which is colocated with a diffraction feature of α Cen B's PSF and is likely a residual speckle artifact. A green circle marks the position of *S*1, which may be associated with an α Cen B diffraction feature but is the only source we confidently redetect in the more robust PCA-KLIP reductions.

S/N map) obtained by combining the reductions conducted in nonoverlapping annuli centered at {1.″5, 2.″5, 3.″5} (Figure 7). *S*1 is redetected at an S/N of 5.4 (corresponding to a 4σ detection). The S/N ratio is converted to a Gaussian detection significance level for the equivalent false positive probability using the `significance` function in `vip_hci`. *A*1 is also seen in the reduction but is not detected at a significant S/N. It is discussed in more detail in the following section.

4.2.2. Robustness of S1 to Varying Point-spread Function Subtraction Geometries and Principal Components

PSF subtraction is performed in the annular mode for varying numbers of subsections ($N_{\rm sub}$), annulus widths, and PCs to test the robustness of the *S*1 candidate. First, we apply joint PCA-KLIP to a four FWHM wide annulus centered at a radial separation of $\approx$1.″5 with no subsections and then divided into two, four, and eight subsections. The number of PCs is automatically chosen by the `pca_annular` function as discussed in Section 4.2.1 for each reduction. Second, we apply joint PCA-KLIP to a three FWHM wide annulus centered at a radial separation of $\approx$1.″5 with no subsections and then divided into two subsections along one of the 4QPM transition boundaries. In each case, we perform multiple reductions by varying the number of PCs used incrementally. Across these reductions, we track the S/N and flux (in a one FWHM diameter aperture) of *S*1 and *A*1. We also examine the S/N and aperture flux of the residual speckle noise at the separation of *S*1, estimated using nonoverlapping one FWHM diameter circular apertures at different PAs.

Performing the first test, we find that *S*1 is recovered irrespective of the number of subsections used (Figure 8). However, *A*1's signal becomes weaker as the number of subsections increases and disappears for the reduction with eight subsections (Figure 8). Performing the second test, for the two $N_{\rm sub}$ cases, we find that *S*1 behaves distinctly from

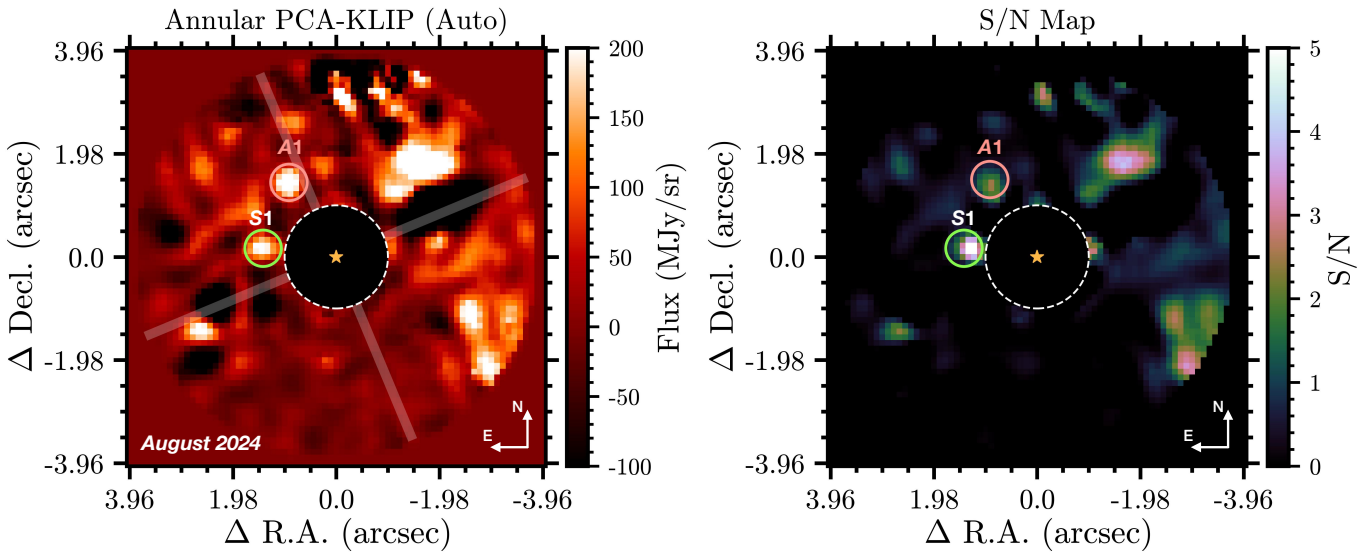

Figure 7. Joint PCA-KLIP subtraction of α Cen AB for the 2024 August observations with automatic PC selection. Left: the de-rotated residual image (north up, east left) after PSF subtraction in three concentric annuli. The MIRI/4QPM transition boundaries are shown as gray shaded regions. Point-source detections of *S*1 and artifact *A*1 (discussed in Section 4.2.2) are circled. Right: S/N map for the reduction shown in the left panel. *S*1 is detected with a peak S/N of 5.4 (4σ). *A*1 is brighter than *S*1 but detected a lower peak S/N of 2.5 (the residual noise estimated using nonoverlapping apertures at the same separation but different position angles (PAs), following D. Mawet et al. 2014, is higher at the separation of *A*1.)

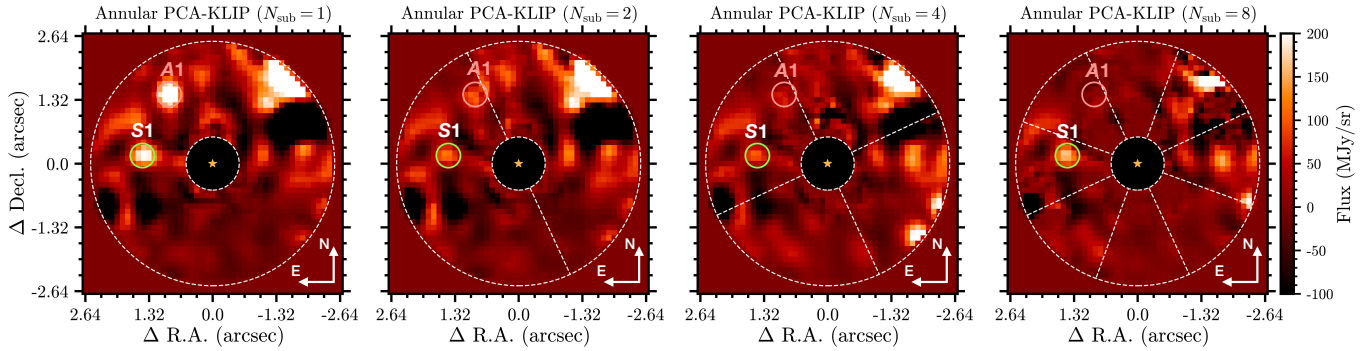

Figure 8. Joint PCA-KLIP subtraction of α Cen AB for the 2024 August observations for different number of azimuthal subsections (N_{sub}). *S*1 is recovered in all reductions, whereas *A*1's signal disappears as N_{sub} increases.

both *A*1 and the residual speckle noise. *S*1's S/N remains relatively flat at values >4 for few PCs and then smoothly decreases as the number of PCs used increases (Figure 9). The aperture flux of *S*1 exhibits a similar behavior. *A*1's flux, on the other hand, starts out higher than *S*1's when using only a few PCs but experiences a drastic drop as the number of PCs is increased ($\gtrsim$150 for $N_{sub}=1$ and $\gtrsim$100 for $N_{sub}=2$; Figure 9). The S/N of *A*1 shows similar behavior as its aperture flux. The S/N of the residual speckle noise at the same separation is <3 and remains roughly flat across PCs.

Together, both tests confirm that *A*1 is a residual artifact from α Cen B's PSF (as first suspected based on the comparison in Figure 6). *A*1 is not robust to changing PSF-subtraction geometries and the rapid flux drop above a critical number of PCs is a telltale sign that it corresponds to a PSF feature that was modeled and subtracted out by PCA-KLIP. For *S*1, the two tests strengthen the case against it being a speckle or α Cen B diffraction artifact. *S*1 is robust to changing PSF-subtraction geometries and the images in Figure 9 show that (1) its flux and S/N evolve smoothly with an increasing number of PCs (the smooth decrease is a feature of oversubtraction with RDI); and (2) it persists as a point source at higher number of PCs after the subtraction of *A*1, which has been directly associated with an α Cen B PSF artifact.

4.2.3. *Detection of* S1 *in Multiple Data Subsets*

To verify that *S*1 is not a detector-level artifact in the α Cen AB integrations, we perform two tests. First, we inspect the mean brightness in a 3 pixel radius aperture centered on *S*1's position in the original, background-subtracted Stage 2 integrations. Sharp increases in the mean pixel brightness (from uncorrected hot pixels, for example) could result in a positive flux artifact at the location of *S*1 after PSF subtraction. The pixel brightness time series shows that there are no such sharp transitions across the α Cen AB integrations (Figure 10). Second, we divide the (1250) α Cen AB integrations into various subsets: first and second half of the data, even and odd frames, and first and last frames. Each subset is reduced independently using joint PCA-KLIP applied to a three FWHM wide annulus centered at a radial separation of $\approx$1.″5 divided into two subsections along one of the 4QPM transition boundaries and using 200 PCs. A detector artifact would appear in some reductions, but not all. Performing this test, we

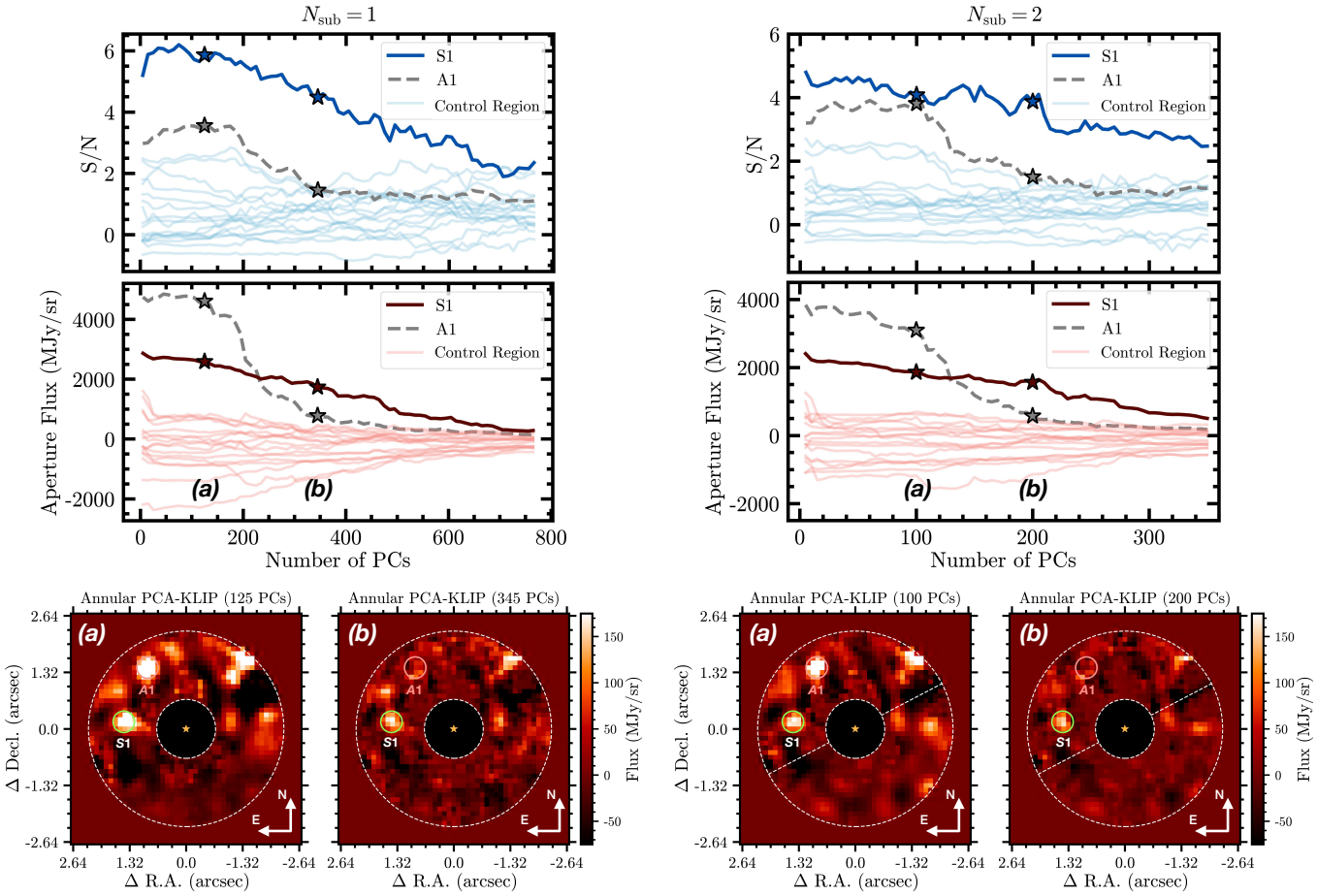

Figure 9. Evolution of *S*1 and *A*1 with the number of PCs used in the joint PCA-KLIP subtraction procedure for the 2024 August observations. The left panel corresponds to reductions where joint PCA-KLIP is applied to a single annulus. The right panel corresponds to reductions where joint PCA-KLIP is applied to a single annulus divided into two subsections. Top row: S/N as a function of of the number of PCs for *S*1 and *A*1. They are compared to the S/N of the residual speckle noise estimated in one FWHM diameter circular apertures at the same separation as *S*1 but at different PAs (control region; each semitransparent line corresponds to an aperture at a different PA). Center row: same as the top row but for the aperture-integrated flux as a function of the number of PCs. Bottom row: two representative postprocessed images at PCs marked by stars in the above figures. *S*1's signal remains stable across PCs, whereas *A*1's signal disappears after a certain number of PCs.

detect *S*1 at a consistent S/N across all subsets (Figure 11). Together, the above two tests show that *S*1 is not likely a detector-level artifact in the α Cen AB integrations.

Interestingly, the above analysis shows that *S*1 can be detected in a single frame of the α Cen AB integration sequence (exposure time of $\approx$7.5 s) with similar S/N. This indicates that the observations are not background limited for the above exposure time. Additionally, the detection of *S*1 at the same position in the first and last integration of the $\approx$2.6 hr sequence shows that that *S*1 is unlikely to be a foreground (solar system) object such as a main-belt asteroid, which at the solar elongation of our observations ($\sim$100°) would have a mean proper motion of $\gtrsim$10 arcsec hr^{-1}. Two other arguments suggest *S*1 is not a solar system object. At a 12 μm brightness level of $\geqslant$ 3 mJy (the flux of *S*1 is $\approx$3.5 mJy at 15.5 μm, see Section 6), there are fewer than 10^{-4} main-belt asteroids in a $5' \times 5'$ field at α Cen A's ecliptic latitude of $\beta = -42°$.[18] Furthermore, the Minor Planet Catalog shows no known objects at the position of α Cen A at the August epoch.[19]

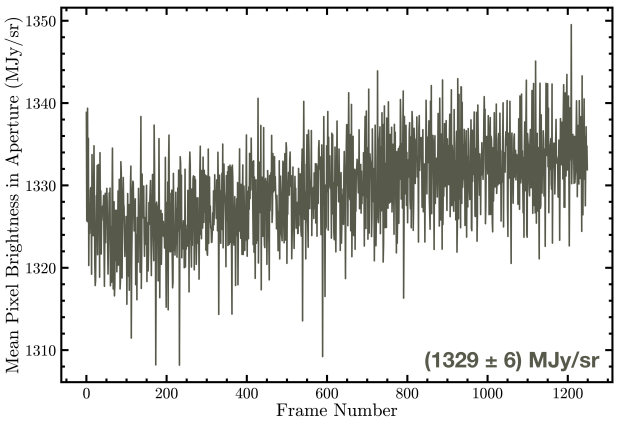

Figure 10. The average pixel brightness in a 3 pixel radius aperture centered on *S*1 in the background-subtracted Stage 2b α Cen AB integrations from 2024 August. The time series does not show any sharp transitions (increases) that would appear as an artifact at the location of *S*1 after PSF subtraction.

4.2.4. "Leave-one-out" Analysis

To verify that *S*1 is not an artifact introduced by any of the ϵ Mus coronagraphic reference images, we perform nine reductions where frames at each dither position of the ϵ Mus

[18] https://irsa.ipac.caltech.edu/data/SPITZER/docs/files/spitzer/asteroid_memo.pdf
[19] https://minorplanetcenter.net/cgi-bin/checkmp.cgi

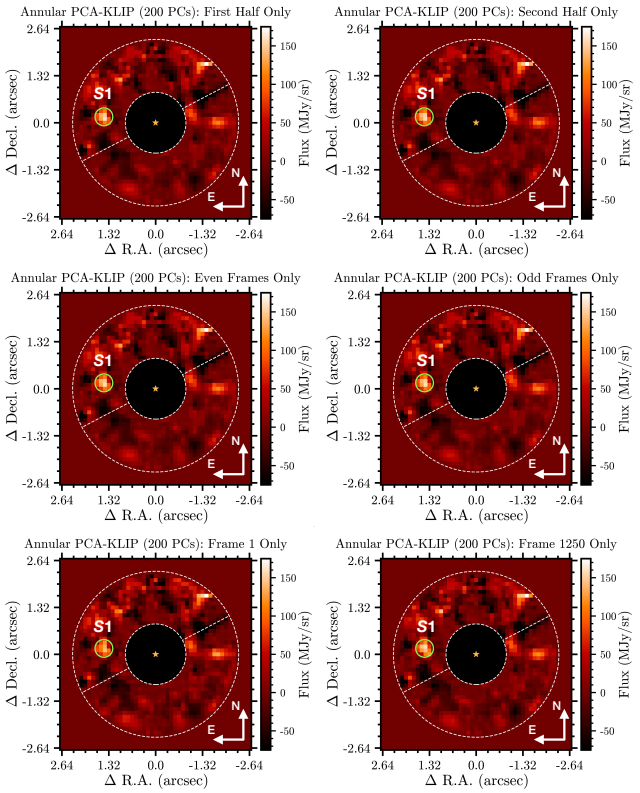

Figure 11. Joint PCA-KLIP subtraction of distinct subsets of the α Cen AB science integrations from the 2024 August observations. Reductions performed on the first half, second half, even set, odd set, first frame, and last frame of the integration sequence are shown from top left to bottom right. *S*1 is consistently detected in all data subsets.

observation are iteratively excluded from the reference library. Each reduction is inspected to ensure that *S*1 is consistently detected in the data. An artifact from the ϵ Mus coronagraphic images would be detected in some reductions, but not all. Performing the test with an identical reduction setup as in Section 4.2.3, we find that *S*1 is detected at consistent S/N across all reductions (Figure 12) showing that it is not likely an ϵ Mus coronagraphic image artifact. A complete summary of all tests is provided in the conclusions (Section 9).

5. 2025 February and April Data Postprocessing

There were three primary goals for the 2025 February and April observations: (1) take advantage of α Cen A's large proper motion ($\mu_\alpha,\ \mu_\delta = -3640, 700$ mas yr^{-1}) to test if *S*1 is a stationary background object; (2) redetect and confirm that *S*1 is an astrophysical source (orbiting planet) and not a residual image artifact; and (3) conduct a new search for additional planets around α Cen A that may be in more favorable orbital locations for detection.

5.1. Is S1 a Background Object?

Using the ephemeris for α Cen A (Paper I), we computed the location of *S*1 with respect to α Cen A at the 2025 February and April epochs assuming it is a stationary background source (Figure 13). We then perform joint PCA-KLIP in an annulus with a width of three FWHMs, centered at the expected radial separation for *S*1 as a background object, with the number of PCs automatically chosen as described in Section 4.2.1. No point source is detected at the expected location of a stationary background source in either epoch (Figure 13). We confirm the sensitivity of our reductions by injecting a synthetic `STPSF` companion model with a flux of 2.5 mJy (1σ lower bound for *S*1, see Table 1) in the α Cen AB science cube, performing PSF subtraction identically as above, and unambiguously recovering the injected source (Figure 13). This is definitive confirmation that *S*1 is not a background source.

5.2. Is S1 Recovered as an Orbiting Planet?

To conduct a comprehensive search for point sources around α Cen A, we perform reductions where joint PCA-KLIP is applied to a single annulus with a radial size of two FWHM ($\approx 1''$) and centered at varying radial separations between $0\farcs75$ and $3\farcs5$ in steps of $0\farcs25$ (12 different reductions). We allow the `pca_annulus` function in `vip_hci` to automatically select the optimal number of PCs for each annulus as the value at which the standard deviation of the residuals (after the subtraction of the PCA approximation) drops below a tolerance value = 0.1. An S/N map is generated for each reduction following the definition in D. Mawet et al. (2014) using the `snrmap` function in `vip_hci`. For the April data set specifically, each roll is reduced independently of the other using both ϵ Mus on-axis dithered observations and only the corresponding ϵ Mus off-axis observation. The de-rotated postprocessed image for both rolls are then averaged to obtain the final reduction.[20]

No significant point sources were detected in our reductions of both the 2025 February and April data sets. We do not recover *S*1 as an orbiting planet in either follow-up epochs. As a summary, we show representative postprocessed images (and the corresponding S/N maps) obtained by combining the reductions conducted in nonoverlapping annuli centered at $\{1'', 2'', 3''\}$ (Figures 14 and 15). A comparison of the reductions for each of the roll observations in April shows that PSF-subtraction artifacts can be identified by their rotation in the sky plane (north up, east left coordinates). True astrophysical sources would remain stationary in each roll's de-rotated image. Overall, we find that the 2025 February and April reductions are less affected by residual artifacts from α Cen B, primarily due to the better matching ϵ Mus off-axis reference observation (Section 3.3). Note that the reduction of the 2025 February data set has been improved over the one presented in A. Sanghi et al. (2025) with more careful preprocessing.

5.3. α Cen B Diffraction Features in 2025 February

Coincidentally, the difference between the telescope V3PA angles for the 2025 February and 2024 August observations of α Cen AB was $181\fdg8$. The α Cen B off-axis PSF is symmetric with respect to a 180° rotation. Thus, its diffraction pattern, as viewed in sky coordinates (north up, east left), will be nearly identical between the two observation dates. Indeed, the two α Cen B diffraction features colocated with *S*1 and *A*1 in the 2024 August observations are also present, at approximately the same location, in the 2025 February α Cen AB observations (Figure 16). If *S*1 is a persistent PSF artifact from α Cen B in 2024 August, it is reasonable to expect a similar

[20] We also tested ADI with the two roll 2025 April data set. However, the mismatch between α Cen A's position behind the mask between the two rolls (see Section 3.2) results in significant residual artifacts, particularly along the 4QPM transition boundaries.

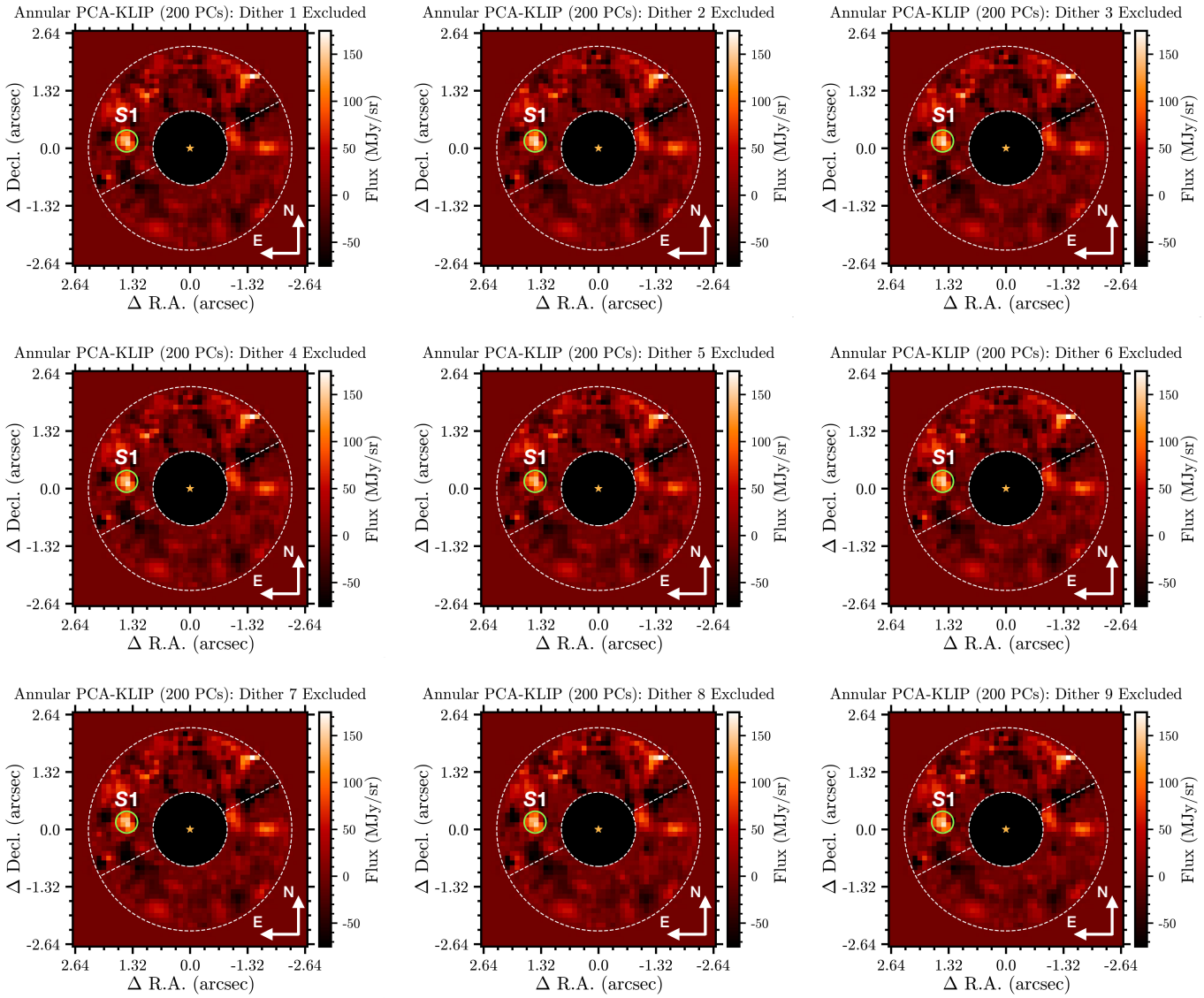

Figure 12. Joint PCA-KLIP reductions for the 2024 August observations where frames at each ϵ Mus dither position are iteratively excluded (one at a time) from the reference library. *S*1 is detected in all reductions indicating that it is not likely an artifact introduced by the ϵ Mus coronagraphic images.

artifact would be created after PSF subtraction in the 2025 February observations. PSF subtraction with the 2025 February observations shows that there is no persistent "*S*1-like" artifact at the location of the α Cen B PSF diffraction feature (Figure 16). An "*A*1-like" artifact is created at very few PCs but is quickly subtracted out as the number of PCs increases (Figure 16). One difference between the 2024 August and 2025 February observations that could impact the interpretation of this analysis is that the February ϵ Mus off-axis reference required a smaller shift to align it with the α Cen B PSF than the corresponding August off-axis reference (see Section 3.3). Nevertheless, the above may be an independent argument against *S*1 being a residual PSF artifact in the 2024 August observations.

6. Astrometry and Photometry of *S*1

Astrometric and photometric measurements of *S*1 are extracted using the negative fake companion injection method (A. M. Lagrange et al. 2010; C. Marois et al. 2010). This technique calibrates measurement biases introduced in the subtraction procedures. We apply this method to the calibrated images in units of MJy sr^{-1} and use the joint PCA-KLIP reduction setup in Section 4.2.3.

First, we simulate a grid of PSF models for the *S*1 candidate accounting for its position with respect to the MIRI/4QPM center using `STPSF` (with the appropriate MIRI filter and mask configuration, using the closest-in-time on-sky OPD map to the observations, and including detector effects). The PSF models are generated at radial separations (ρ) between 12.5 and 14.5 pixels (0.″11 pixel^{-1}) in steps of 0.5 pixels and PAs (θ, measured east of north) between 78° and 88° in steps of 0.°5. The `STPSF` models are normalized to the exit pupil of the optical system so that the sum of the PSF is 1 in an infinite aperture. The source throughput behind the MIRI coronagraph in F1550C at each position is estimated using `STPSF` simulations. We compute the ratio of integrated flux for a model PSF generated with and without the 4QPM inserted in the optical path at the given (ρ, θ) position transformed to the detector frame.

Next, we iteratively inject negative copies of the simulated `STPSF` (with fluxes f ranging from 1 to 5 mJy in steps of

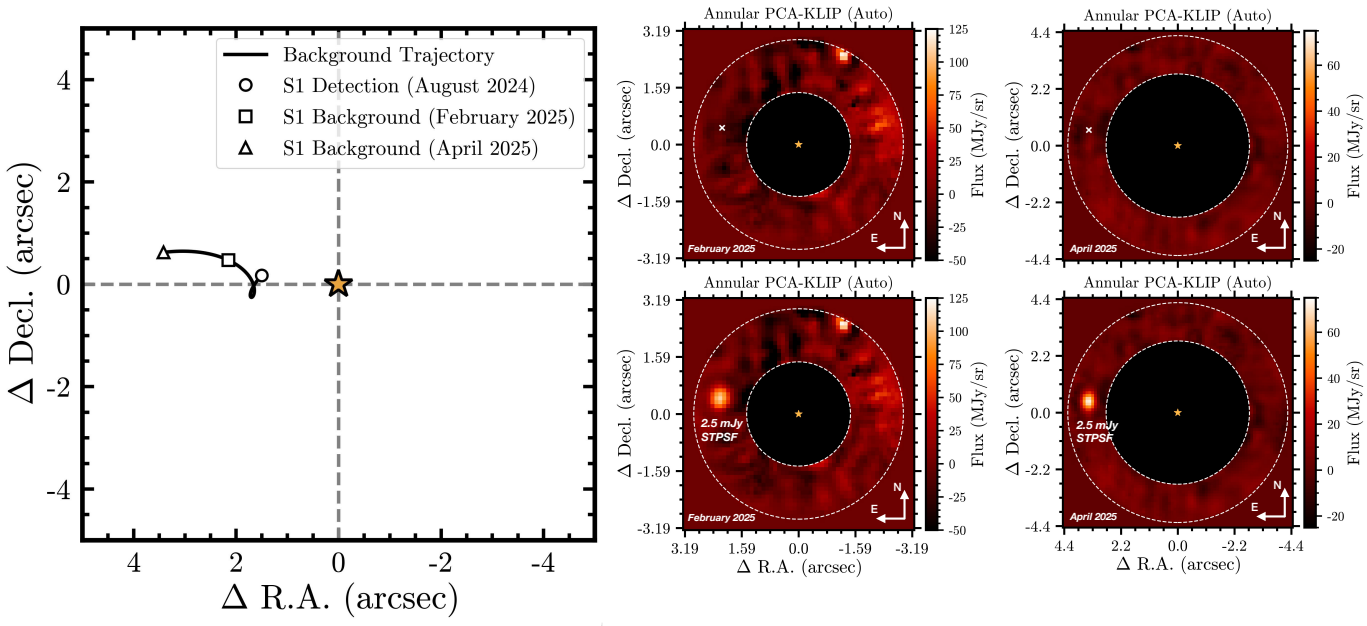

Figure 13. Left: sky motion of *S*1 (with respect to α Cen A marked with a star symbol), as seen by JWST, assuming it is a stationary background source. The square and triangle symbols mark the expected location of *S*1 for the 2025 February and April observation dates, respectively. Right: joint PCA-KLIP reductions for the two epochs showing the nondetection of a point source at the expected location for a background object (marked with a cross, top panel). Injection and recovery of a 2.5 mJy `STPSF` model (bottom panel) confirms the sensitivity of the observations to *S*1. *S*1 is not a stationary background object.

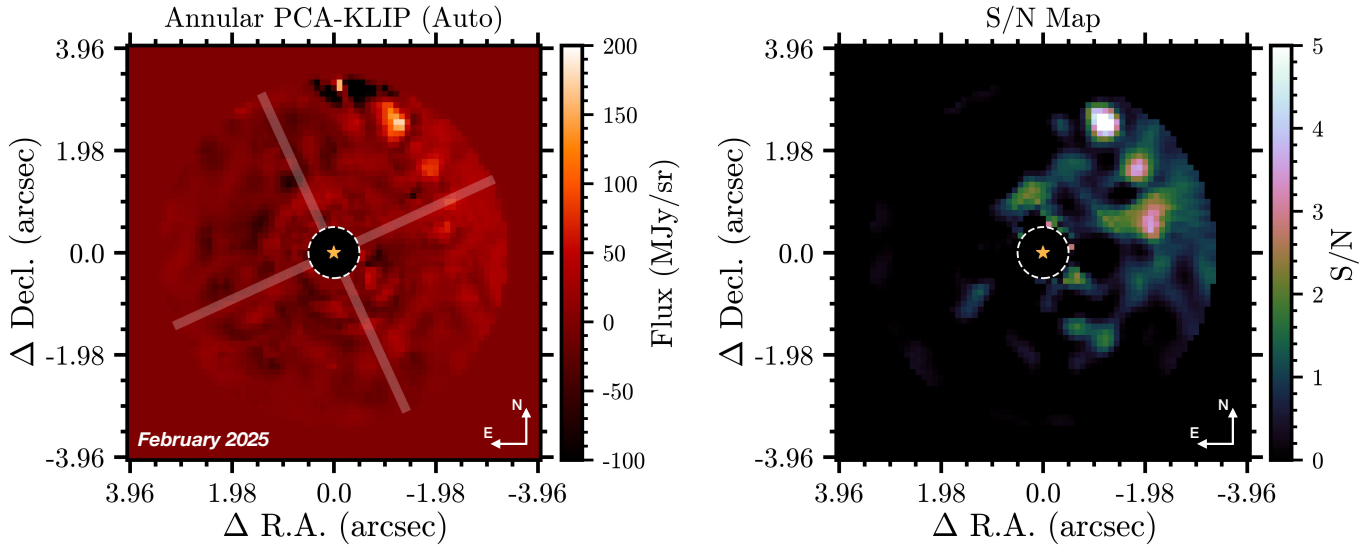

Figure 14. Joint PCA-KLIP subtraction of α Cen AB for the 2025 February observations with automatic PC selection. Left: the de-rotated residual image (north up, east left) after PSF subtraction in three concentric annuli. The MIRI/4QPM transition boundaries are shown as gray shaded regions. Right: S/N map for the reduction shown in the left panel. No significant point sources are detected.

Table 1
Astrometry and Photometry of *S*1

ρ (arcsec)	θ (degrees east of north)	ΔR.A.[a] (arcsec)	Δdecl.[a] (arcsec)	$T_{\rm F1550C}$	$f_{\rm F1550C}$ (mJy)
1.51 ± 0.13	83.5 ± 4.9	1.50 ± 0.13	0.17 ± 0.13	0.75	3.5 ± 1.0

Note.
[a] ΔR.A. and Δdecl. are analytically computed from the estimated (ρ, θ) value. A positive ΔR.A. is east and a positive Δdecl. is north.

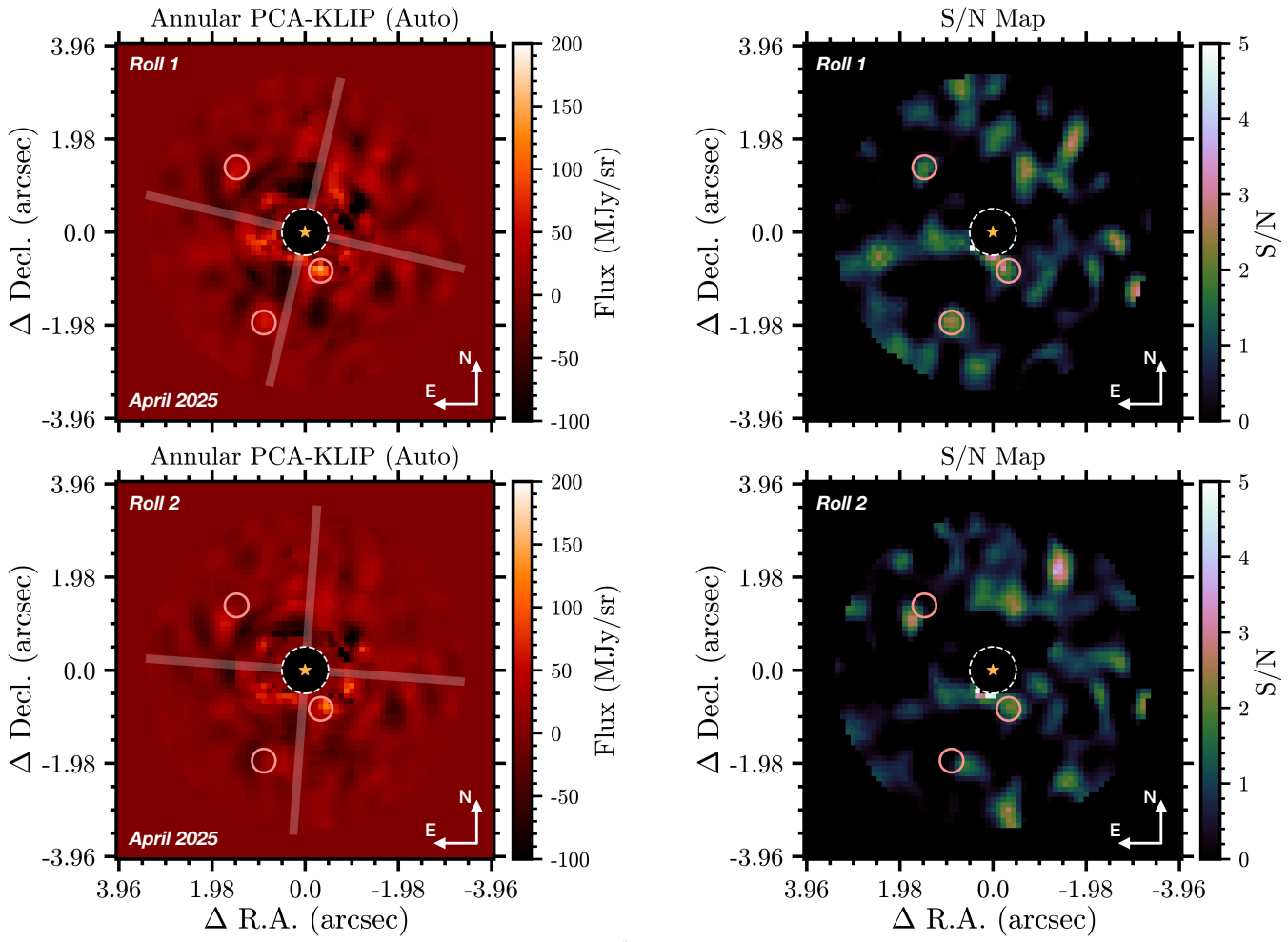

Figure 15. Joint PCA-KLIP subtraction of α Cen AB for the 2025 April observations with automatic PC selection. Left column: the de-rotated residual image (north up, east left) after PSF subtraction in three concentric annuli for each roll observation. The MIRI/4QPM transition boundaries are shown as gray shaded regions. Circular apertures are drawn centered on a few visually distinct features in the roll 1 reduction and at the same location in the roll 2 reduction. The features are present in the roll 2 reduction but offset in PA (matching the direction of the V3PA angle change between the two rolls) from their roll 1 location indicating that they are PSF-subtraction artifacts. Right column: S/N map for the reductions shown in the left column. No significant point sources are detected.

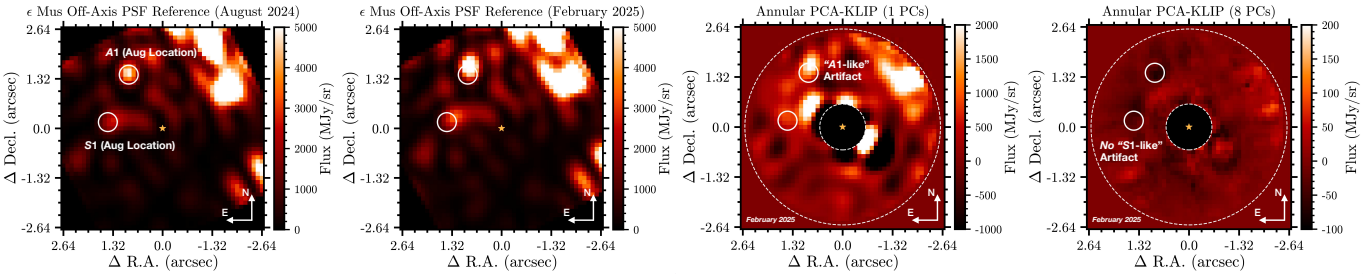

Figure 16. Left: the de-rotated off-axis ϵ Mus reference for α Cen B for the 2024 August observations. It acts as a proxy for and shows the diffraction features expected from α Cen B in vicinity of α Cen A. The locations of the detections of $S1$ and $A1$ in 2024 August are marked. Center left: the de-rotated off-axis ϵ Mus reference for α Cen B for the 2025 February observations. The diffraction pattern is nearly identical to that observed in 2024 August. Center right: joint PCA-KLIP reduction of the 2025 February data set with one PC showing the presence of an "$A1$-like" artifact. Right: joint PCA-KLIP reduction with eight PCs showing that no persistent artifacts are seen at the location of $S1$ (and $A1$).

0.25 mJy, accounting for coronagraph throughput)[21] at each grid point into the background-subtracted α Cen AB integrations, perform joint PCA-KLIP subtraction with identical parameters as in Section 4.2.3, and calculate the RSS of pixel values in a fixed 1.5 FWHM diameter aperture, centered on the visually approximated centroid of $S1$. Once we have obtained the RSS for each (ρ, θ, f) grid point, we marginalize the 3D distribution of RSS values across each axis to obtain the distribution of RSS as a function of separation, PA, and flux (Figure 17). The RSS follows a parabolic function of the injected separation, PA, and flux, which is the expected outcome when the measurement biases are caused by

[21] The flux in units of MJy sr^{-1} is corrected for coronagraph throughput T and converted to units of mJy as: f [mJy] $= f$ [MJy sr^{-1}] $\cdot\, T^{-1} \cdot$ PIXAR_SR [sr pixel^{-1}] $\cdot\, 10^9$, where PIXAR_SR $= 2.86 \times 10^{-13}$ sr pixel^{-1}.

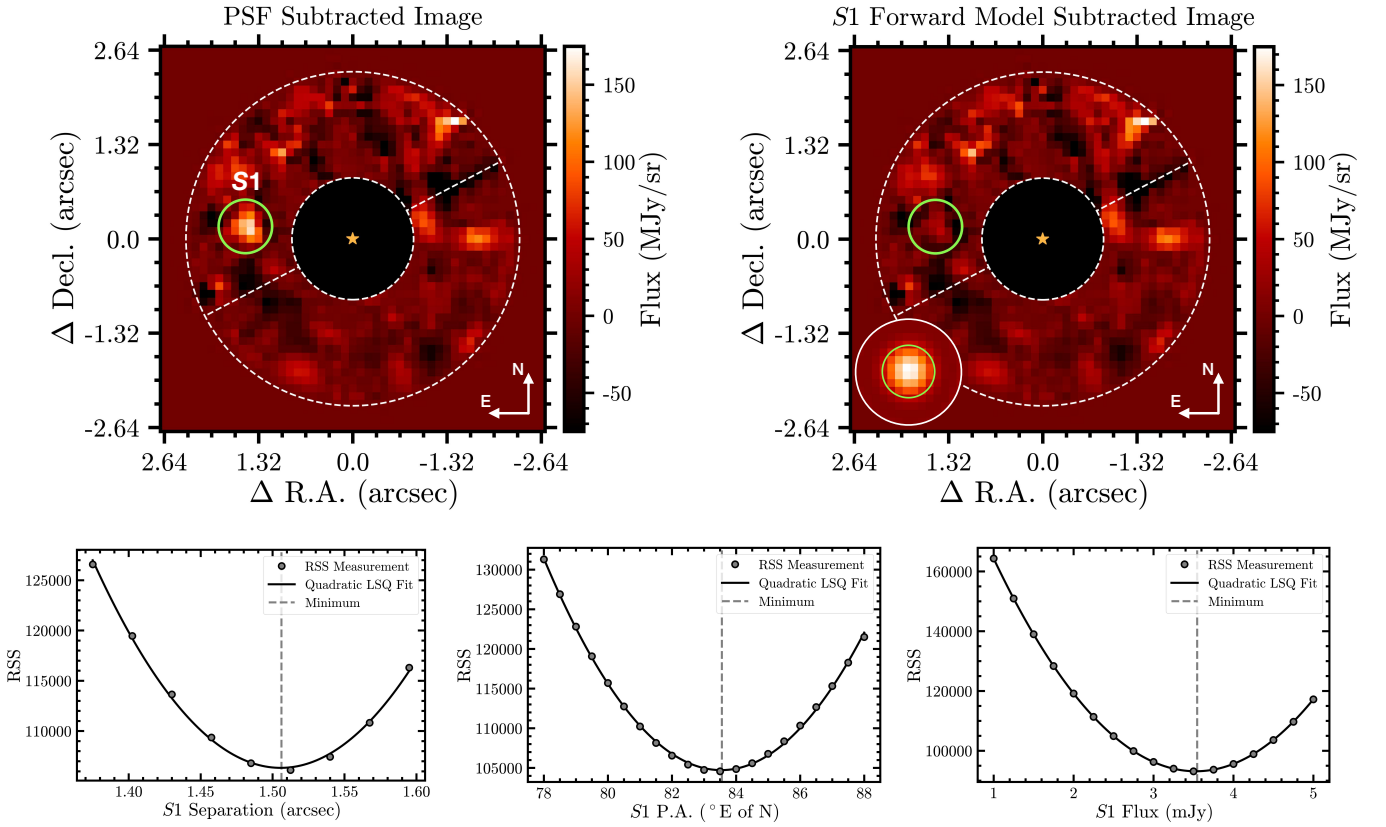

Figure 17. Top panel: the PSF-subtracted image obtained before (left) and after (right) the injection of a negative copy of the best-fit `STPSF` forward model for *S*1. The reduction parameters are identical between the two images. The `STPSF` model injected into the background-subtracted Stage 2 α Cen AB integrations is pictured in the bottom left corner of the right image. The 1.5 FWHM diameter circular aperture where the RSS is minimized is drawn for reference. Bottom panel: marginalized RSS distributions as a function of injected model separation (left), PA (center), and flux (corrected for coronagraph throughput, right). The RSS distributions are well fit by quadratic functions and the minimum corresponds to the forward modeled parameters.

oversubtraction (D. Apai et al. 2016; L. Pueyo 2016; Y. Zhou et al. 2021; A. Sanghi et al. 2022). We perform a quadratic least squares fit to the measurements and use the minimum of each best-fit parabola as the final measurements for the separation, PA, and flux density of *S*1 (Table 1). The best-fit `STPSF` model cleanly subtracts *S*1's signal as seen in Figure 17. This shows that *S*1 is well represented as a point source.

The photometric uncertainty consists of four components: the speckle noise (σ_{sp}), the photon noise (σ_p), the read noise (σ_r), and a PSF normalization uncertainty (σ_n). All uncertainties are quoted as a fraction (in percent) of the point-source flux. The speckle noise is estimated as the standard deviation of integrated flux in a series of nonoverlapping 1.5 FWHM diameter apertures (same size as used for flux estimation of *S*1) constructed at the radial separation of *S*1 in the final joint PCA-KLIP PSF-subtracted image. We find that the speckle noise is ≈25%. The photon and read noise are estimated across pixels in a 1.5 FWHM diameter aperture centered on *S*1 (in the detector frame) by appropriately combining the per-pixel variance provided in the `VAR_POISSON` and `VAR_RNOISE` extension images in the background-subtracted Stage 2 data product. These two terms are negligible (>50× smaller than the speckle noise). Finally, the PSF normalization uncertainty is associated with conversion from detector units of DN s^{-1} to physical units of MJy sr^{-1}. We adopt an uncertainty of 11% based on the results in M. Mâlin et al. (2025). We assume the above sources of uncertainty are independent and take the final uncertainty on the photometry as the quadratic sum of the two dominant terms: $\sigma_f = \sqrt{\sigma_{sp}^2 + \sigma_n^2}$. For astrometric uncertainty estimation, we assume the radial and tangential directions are independent and calculate their uncertainties as FWHM/(S/N) =0.″5/4 ≈ 0.″13. We note that the error in stellar position behind the MIRI/4QPM is ∼10 mas (Section 3.2), which is negligible compared to the above uncertainty. The final results are presented in Table 1. Additionally, we note that *S*1's astrometry and photometry were independently verified using the `pyKLIP` package (J. J. Wang et al. 2015; L. Pueyo 2016; J. J. Wang et al. 2016) and confirmed to be consistent between the joint PCA-KLIP reduction and the classical median-RDI reduction.

7. Point-source Sensitivity Analysis

7.1. Injection–Recovery Procedure

We perform PSF injection–recovery tests with `STPSF` models to characterize the flux and contrast sensitivity of our observations. PSF injections are carried out over the following grid, defined in polar coordinates: $\rho \in$ [0.″75, 3.″5] in steps of 0.″25 and $\theta \in$ [0°, 350°] in steps of 10°. We report our sensitivity as (a) the point-source flux detectable at an S/N = 5; and (b) the point-source flux detectable at a 5σ significance level. We use `vip_hci`'s `significance` function to calculate the S/N (accounting for small sample statistics) that corresponds to a 5σ Gaussian detection significance (for the equivalent false positive probability, ∼3 × 10^{-7}) at each radial

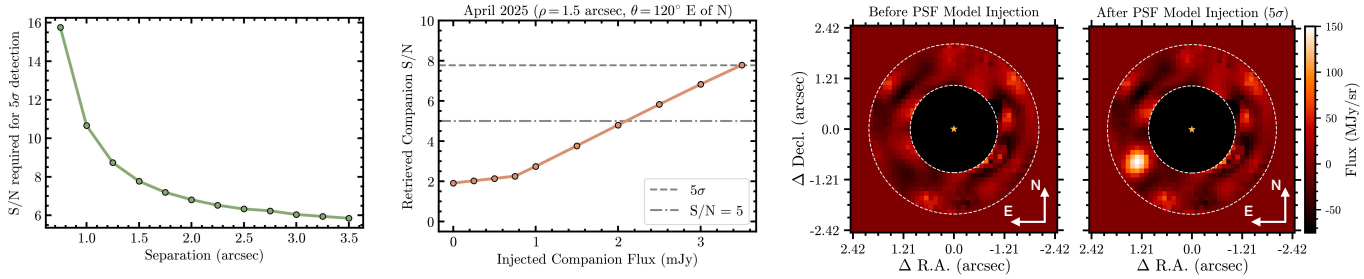

Figure 18. Illustrative example of the injection–recovery procedure. Left: the S/N corresponding to a 5σ detection for the radial separations at which synthetic companions are injected. Center: S/N of a synthetic companion injected at a given (example) position as a function of flux. The 5σ and S/N = 5 detection thresholds are marked with horizontal dashed and dashed–dotted lines, respectively. Right: PSF-subtracted images before and after the injection of the model PSF corresponding to a 5σ detection (≈3.5 mJy in this case).

separation of injection (Figure 18). The S/N = 5 and 5σ flux sensitivities are converted to contrast sensitivity by dividing by α Cen A's flux in the F1550C filter ($f_* = 63$ Jy; Paper I). To determine the sensitivity at a given (ρ, θ), the general procedure for all three data sets is as follows.

1. Inject an `STPSF` companion model generated for the appropriate position on the MIRI detector, filter and mask configuration, using the closest-in-time on-sky OPD map, including detector effects, and scaled to a flux f in units of mJy (after correcting for throughput behind the 4QPM coronagraph at the injection location).
2. Perform a joint PCA-KLIP reduction in an annulus with a width of two FWHM centered at the injection separation with the number of PCs automatically chosen, as discussed in Section 4.2.1. For the April observations, each roll is reduced independently and the PSF-subtracted images are averaged to obtain the final detection image.
3. Estimate the S/N at the location of injection, accounting for small sample statistics.
4. Repeat step 3 for multiple values of f and identify the companion flux for which the target S/N computed earlier is achieved (Figure 18).

We note here modifications made to the above procedure for the 2024 August and 2025 February observations, which were impacted by contamination from α Cen B's PSF in the vicinity of α Cen A. The ϵ Mus off-axis reference in the 2024 August observation required an ≈3 pixel shift to align it with α Cen B (Section 3.3). This results in an imperfect subtraction of α Cen B (specifically, for the brightest diffraction features) and generates several artifacts in the northwest quadrant of the image (see Figure 7, for example), which impact the detectability of point sources in the region and bias the S/N calculations for injected sources at other PAs. Thus, we exclude this area (PA =290°–20°) from the injection–recovery tests for all injection separations. Similarly, the 2025 February reductions are affected by a residual subtraction artifact from α Cen B at PAs between 330°–0° (see Figure 14, for example) for separations $\geqslant 2\farcs75$. This area is excluded from the injection–recovery tests. In both cases, the noise estimation for the S/N calculations of the injected sources at other PAs is conducted using apertures that do not fall in the excluded region. In principle, we could manually tune (increase) the number of PCs to better subtract the residual α Cen B artifacts (as can be seen from comparing the low and high PC reductions in Figure 9; see also the discussion in Appendix A). However, this is impractical to implement given the number of injection–recovery tests being conducted.

7.2. Two-dimensional Sensitivity Maps

From the above analysis, we found that the sensitivity to companions in the vicinity of α Cen A can vary significantly as a function of spatial position due to the complex nature of the underlying speckle field (e.g., because of the absence of a second roll angle observation and/or the contaminating presence of α Cen B) and the effect of the 4QPM transition boundaries. Thus, we report our S/N = 5 and 5σ sensitivities in the form of 2D maps (Figure 19). For a few injection locations in each of the epoch observations, we were unable to accurately determine a sensitivity. Three reasons were (1) the S/N threshold for 5σ detection was not met, even for low contrast ($\sim 10^{-1}$) injections (primarily at a $0\farcs75$ separation, which requires S/N ≈ 16 for a 5σ detection, Figure 18); (2) the presence of a known PSF-subtraction artifact at the injection location positively biased the flux and led to a significantly deeper S/N = 5 flux sensitivity estimate than appropriate; and (3) in the case of the 2024 August observations, injections near the location of $S1$ were biased. All of the above cases were identified by inspecting the PSF-subtracted images for the different flux levels of injection at each position. We do not report sensitivities at these locations. The final 2D sensitivity maps are constructed by transforming the polar coordinate grid to a rectangular grid and linearly interpolating the sensitivity values (using `scipy.interpolate.griddata`) at a resolution of $0\farcs11$ pixel^{-1} (equal to the MIRI detector plate scale). While it is most accurate to use the 2D map for sensitivity analyses, we also present traditional 5σ (and S/N = 5) median flux and contrast curves (Figure 19) as they are commonly used in the literature. We compute the median (azimuthally averaged) contrast as a function of separation. We also present the azimuthal minimum sensitivity as a function of radial separation.

The 2D sensitivity maps (Figure 19) show remarkable variation between the various observation epochs. The 2024 August maps are nonuniform, with the sensitivity achieved being highly dependent on the exact location in the image. This is a consequence of the higher contamination from α Cen B due to its imperfect subtraction. The 2025 February maps are more uniform and demonstrate better sensitivity to point sources compared to 2024 August because of the improved subtraction of α Cen B. The sensitivity is relatively flat at separations $> 2''$ (see the contrast curve). The 2025 April maps are uniform, radially striated, and achieve deeper sensitivity than the 2025

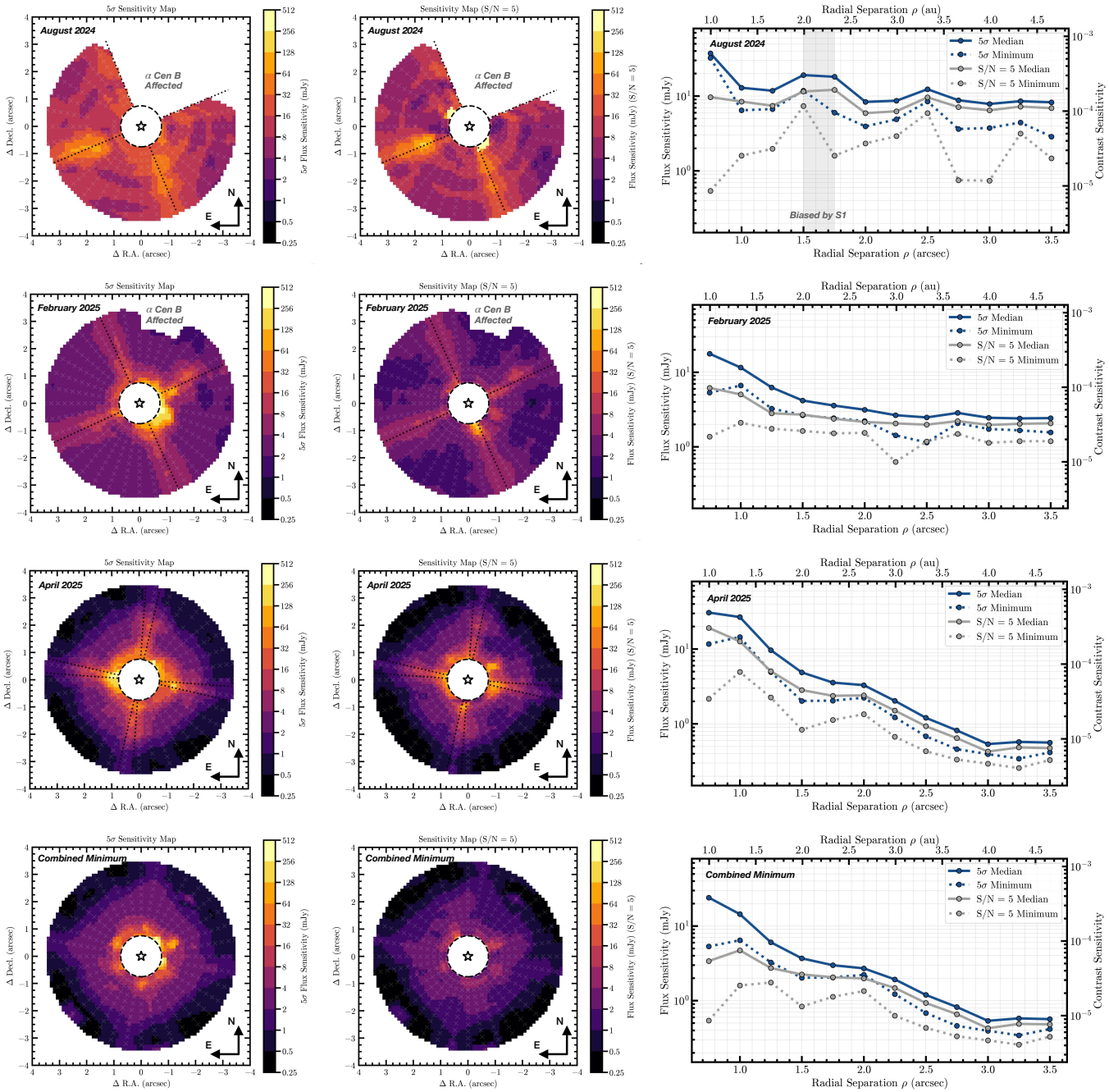

Figure 19. Results of the injection–recovery analysis with the α Cen AB data. Left column: 2D 5σ flux sensitivity maps for each of the three epochs of observation, and their combined minimum, in sky coordinates (north up, east left). The central region ($<0\farcs75$, or <1.5 FWHM, radial separations) is masked (poor detectability). The dotted lines correspond to the orientation of the 4QPM transition boundaries (one for each roll in 2025 April). The regions excluded from the injection–recovery analysis in the 2024 August and 2025 February observations due to contamination from α Cen B are labeled. The crosses mark the (ρ, θ) grid points where sensitivity was estimated. A discrete color map is chosen to highlight the different sensitivity zones across the image. Center column: same as the left column but for the S/N = 5 flux sensitivity. Right column: 5σ and S/N = 5 median and minimum flux–contrast curves for each epoch. The median and minimum flux–contrast are both computed over all PAs of injection for a given separation from the 2D sensitivity maps.

February observations at separations $> 2''$. The biggest reason for this difference is the significantly lower contamination from α Cen B due to its orientation in the detector plane (see Figure 1). The availability of two roll angles of observation also contributes to the improved sensitivity. A comparison of the contrast curves shows that the 2025 February observations achieve better sensitivity than the 2025 April observations at separations $< 1\farcs25$. At close-in separations, the latter epoch is compromised by residual artifacts from the PSF subtraction (see Figure 15). A common feature across all the maps is the poor sensitivity along the 4QPM transition boundaries, as expected, because of the low planet throughput. Our observations typically reach a 5σ sensitivity better than 4 mJy corresponding to contrast ratios deeper than 6×10^{-5} for separations $\gtrsim 1\farcs5$. Our best sensitivities are $\lesssim$2 mJy corresponding to contrast ratios deeper than 3×10^{-5} for separations $\gtrsim 1\farcs5$. The above are comparable to, and in some cases better than, those achieved for single star F1550C observations with JWST/MIRI (e.g.,

A. Boccaletti et al. 2022; M. Mâlin et al. 2025; E. C. Matthews et al. 2024). In general, at the above separations, the F1550C observations are background limited (A. Boccaletti et al. 2022). The improvement in contrast sensitivity over past observations is because of the lower background limit given the bright stellar magnitude of α Cen A. The 5σ and $S/N = 5$ sensitivities differ by about a factor of 2 at separations $< 1\farcs25$ and the difference is lower for larger separations. As a summary, we also present an epoch-combined sensitivity map (Figure 19), showing the best sensitivity across epochs at a given injection location, and the corresponding contrast curves. It is important to note that the sensitivities presented for all three epochs are conservative (particularly 2024 August). Better sensitivity can be achieved by manually tuning (increasing) the number of PCs used to improve the suppression of subtraction artifacts generated by both α Cen A and α Cen B (as was done to test the robustness of the *S*1 candidate in Section 4.2.2 and demonstrated in Appendix A). As noted earlier, this is not practically feasible for our injection–recovery tests.

Overall, the above analysis highlights the importance of observing a system like α Cen AB, where the sensitivity achieved is inconsistent between different observations (due to the unique binary astrophysical scene), at multiple epochs to improve completeness to planets that may be located at unfavorable locations (e.g., near the transition boundary, within the inner working angle, or at the locations of artifacts) in any single epoch. The individual epoch sensitivity maps are particularly important in the context of α Cen AB as they constrain the orbits of candidate *S*1 that are consistent with nondetections in 2025 February and 2025 April. All individual epoch (interpolated) 2D sensitivity maps presented in this Letter, as well as the sensitivities at the individual (ρ, θ) grid points where the PSF injection–recovery tests were performed, are available at doi: 10.5281/zenodo.15748931. The orbital analysis, along with a translation of the achieved flux sensitivity to detectable planet scenarios (effective temperature and radius), is presented in Paper I.

8. Search for and Limits on Exozodiacal Emission

We investigate the detectability of faint, spatially extended exozodiacal emission in the α Cen AB system in the 2025 February and April epochs. This section introduces our analysis framework, including an empirical approach to estimating detection significance, which we also use in injection–recovery tests to quantify sensitivity to varying levels of exozodiacal emission.

8.1. Signal-to-noise Ratio Map Calculation

To evaluate the presence of a potential signal in both the original and model-injected data, we compute the S/N in a certain aperture across a grid of predefined aperture geometries, hereafter referred to as the S/N map. The target aperture geometry is motivated by the expected morphology of an inclined exozodiacal disk and consists of a star-centered rectangle, as illustrated in Figure 20. By systematically varying the aperture's length and orientation, we compute the S/N map, as detailed in the steps below.

1. We integrate the flux inside a given target aperture (signal region), which is defined as a rectangle with a width of $1''$ (≈two FWHM) and an overall length of $3\farcs8$–$6''$, with a central region of radius $= 1\farcs3$ masked to avoid residual PSF-subtraction artifacts. Converted to projected distance from α Cen A, our aperture stretches roughly from 1.7 au at the inner boundary out to 2.4–4 au.
2. We then place another aperture orthogonal to the target aperture to determine the background and noise levels. This aperture has the geometry of two opposing annulus sectors, each with a radial extent equal to the target aperture handles, and an angular extent of 120° (Figure 20).
3. The S/N is computed using the formula S/N = (signal − background)/noise.
4. We repeat steps 1–3, varying the PA of the target aperture from 0° to 180°, as well as the target aperture length from $3\farcs8$ to $6''$.

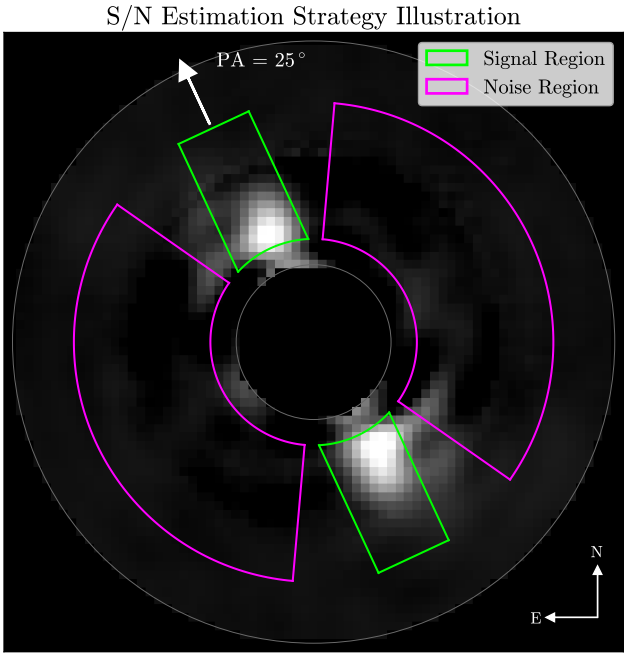

Figure 20. Illustration of how the S/N map is generated for the detection of extended emission. The figure shows an example of a signal region (green) at one PA, along with the corresponding perpendicular annular noise region (purple), using the coplanar asteriod belt analog (ABA) ABA-1 exozodi model injected into the April data. The S/N is calculated by varying the aperture's PA and length.

For both the 2025 February and April observations, we mask a $0\farcs5$ wide corridor centered on the MIRI 4QPM transition boundaries when computing the S/N maps. Additionally, for the 2025 February observations, we mask the northwest region that is impacted by residuals from α Cen B's PSF. Note that we are not using any prior knowledge about any potential (or injected) disk properties (PA or size) in our calculations.

8.2. Signal-to-noise Ratio of Extended Emission in the Original Data

The 2025 February and April epoch observations are the two best data sets to search for extended emission given the better matching reference for and subtraction of α Cen B (see Sections 3.3 and 5.2, and Figure 19). Unlike a close-in orbiting planet, the properties of extended emission features are not

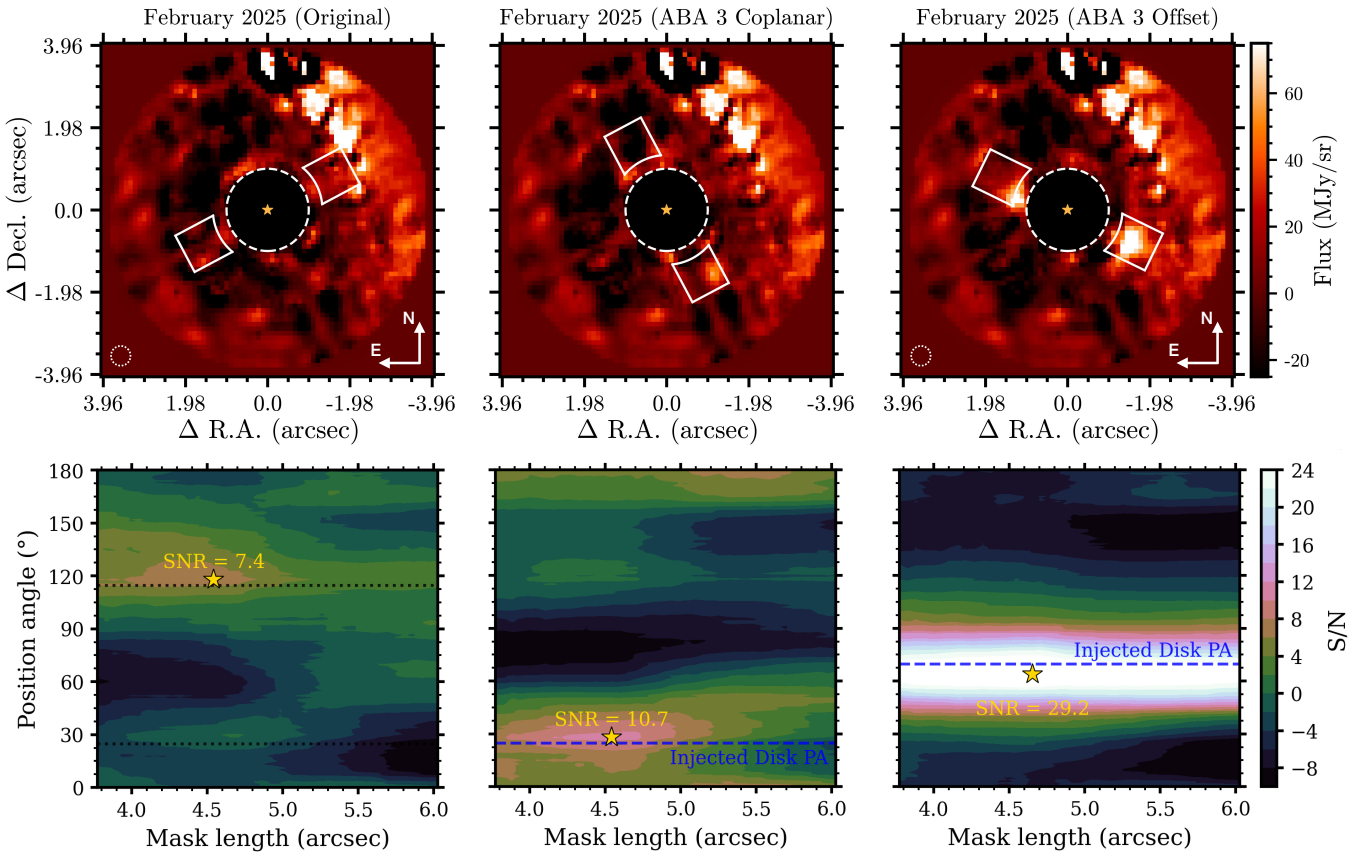

Figure 21. PSF-subtracted images (top) and the corresponding extended emission S/N maps (bottom) for the 2025 February observation for three cases: (left) original data, (center) ABA-3 exozodi model injected with a coplanar orientation, and (right) ABA-3 exozodi model injected with an offset orientation. In the image plots, a one FWHM diameter beam is indicated in the bottom left corner with a dotted circle. The aperture that yields the highest S/N (marked by a star in the S/N maps) is shown in the images. For the original data, dotted lines in the S/N map mark the PAs of the 4QPM transition boundaries. For the injected cases, dashed lines mark the PAs of the injected disks.

expected to change between observations on a 1 yr timescale. Hence, we focus our reduction efforts on the 2025 February and April epoch observations. For each epoch, we perform a single reduction where joint PCA-KLIP is applied in two concentric annuli each with a radial size of three FWHM ($\approx 1\farcs5$), centered at radial separations of $\{1\farcs75, 3\farcs25\}$, and with the number of PCs automatically selected as described in Section 4.2.1. The central two FWHM radius region is masked. For the April data set, each roll is reduced independently and then the postprocessed images are stacked. An S/N map across aperture geometries is generated for each epoch following the method described in the previous section. The results are shown in the left columns of Figures 21 and 22.

The peak S/N is 7.4 for the February observations and 5.0 for the April observations. To assess detection significance, we define an empirical S/N significance, σ, by normalizing each peak S/N value by the 68.3 percentile of the absolute S/N distribution in the respective PSF-subtracted images. This threshold represents the empirical 1σ level of background fluctuations under the full measurement process, including the effects of correlated noise, and is $\mathrm{S/N}_{1\sigma} = 3.5$ and $\mathrm{S/N}_{1\sigma} = 3.8$ for the 2025 February and April data, respectively. We then define a detection as a significance threshold of $\sigma > 3$, i.e., $\mathrm{S/N}_{3\sigma} \approx 11$, in both cases. It thus follows that no significant extended emission features are detected in either epoch. We note that the PA along which the peak S/N is obtained in the 2025 February image coincides with one of the 4QPM transition boundaries. Additionally, the peak S/N in the 2025 April image is biased by a residual PSF-subtraction artifact (Figure 22), rather than arising from disk emission, as was verified by the rotation of the feature between the reductions for each roll in the sky orientation (north up, east left). A true astrophysical disk would remain fixed in sky orientation between the two rolls.

8.3. Signal-to-noise Ratio with Injected Disks

We investigated the sensitivity of the 2025 February and April epoch observations by injecting five exozodi disk models at two geometries: four ABA models and a fiducial "1-zodi" model, at coplanar and offset geometries, respectively. The input physics and model calculation procedures are described in Paper I. In summary, we first simulate surface brightness distributions for different disks, considering (1) a set of ABA models, in which dust is collisionally produced in a narrow belt and transported inward via Poynting–Robertson drag (following J. K. Rigley & M. C. Wyatt 2020), and (2) a solar system analog based on the T. Kelsall et al. (1998) zodiacal cloud model, placed around α Cen A. For the ABA models, we vary the belt mass across four levels (ABA-1 to ABA-4), where ABA-1 corresponds to the most massive and brightest disk, and ABA-4 to the least massive and faintest disk. We then synthesize 4QPM coronagraphic observations of the inclined disks (following M. Sommer et al. 2025), for injection into our data sets. Relevant to the analysis presented here, the

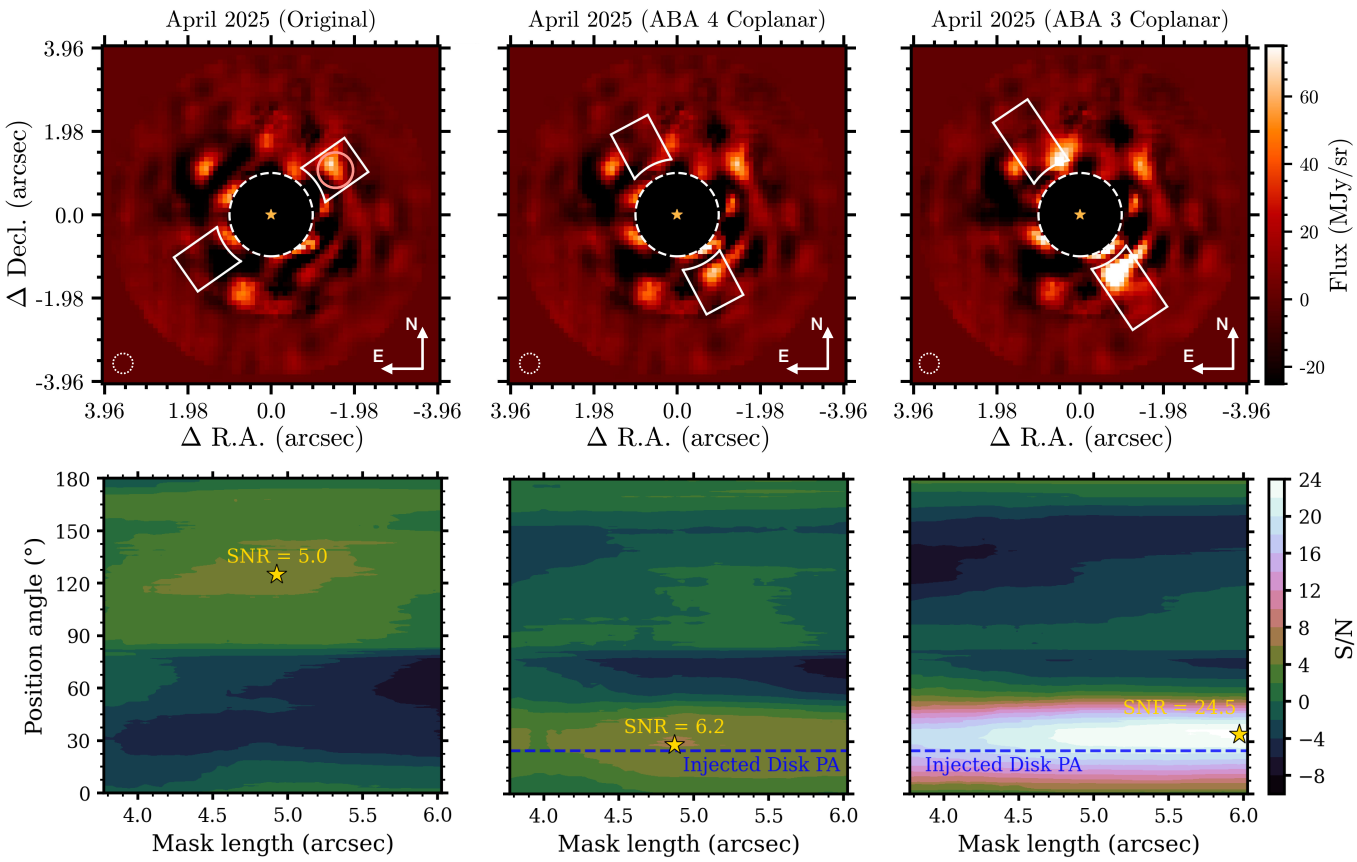

Figure 22. Same as Figure 21 but for the 2025 April observations. Here, the injected cases shown are the ABA-4 and ABA-3 models, both in the coplanar orientation. In the image showing the original data (top left), a solid circle marks a suspected PSF-subtraction artifact (see the text).

coplanar geometry refers to an exozodi model with the same inclination and PA as the α Cen AB binary. The offset geometry refers to an exozodi model with the same inclination as the α Cen AB binary but offset in PA by 45°, counterclockwise. We note here that the coplanar orientation falls along the 4QPM transition boundary for the 2025 February observations (but not the 2025 April observations). The offset geometry models were generated to quantify the sensitivity level in regions not impacted by throughput loss due to the transition boundaries for the 2025 February epoch.

We iteratively injected each exozodi model, at each geometry (5 × 2), into the original α Cen AB integrations (for each epoch), performed the same joint PCA-KLIP reduction described in the previous section, and again computed the S/N map across the search aperture geometries, as well as significances with respect to the $S/N_{1\sigma}$ from the original data, as described in Sections 8.1 and 8.2. Table 2 summarizes the retrieved S/N and empirical significance for each model injection case for both epochs. We find that the exozodi ABA-3 models are brighter and consistently above or near the detection threshold. In the April 2025 observation, the ABA-4 model is not detected, whereas the ABA-3 model is readily detected (Figure 22). The 3σ threshold is narrowly missed in the February epoch for the coplanar disk. This is because, in that epoch, the 4QPM transition boundary aligns precisely with the disk and significantly attenuates its flux. This is illustrated in Figure 21, showing the injected images and S/N maps for the coplanar as well as the offset ABA-3 model.

Overall, our injection–recovery tests place upper limits of $Z_L \lesssim 5$ zodis and $Z_\Sigma \lesssim 8$ zodis (ABA-3 model, Table 2) on the presence of (coplanar) exozodi emission around α Cen A. This level of sensitivity is remarkable: >5–10× deeper than the current best limits achieved with nulling interferometry using the Large Binocular Telescope Interferometer (S. Ertel et al. 2018, 2020). The primary reason for the above gain in sensitivity is JWST's ability to resolve α Cen A's habitable zone (due to the star's proximity) and JWST's excellent stability, which allows us to accurately subtract the stellar contribution and achieve deep contrast performance. A detailed discussion of the implications of this upper limit is presented in Paper I.

9. Conclusions

We conducted JWST/MIRI F1550C coronagraphic imaging observations of our closest solar twin, α Cen A, over three epochs between 2024 August and 2025 April to directly resolve α Cen A's habitable zone and perform a deep search for planets and exozodiacal disk emission. In this Letter, for the first time with JWST, we demonstrated the application of RDI to simultaneously subtract the coronagraphic image of a primary star (α Cen A) and the PSF of its binary companion (α Cen B). The postprocessing strategies used in this work were specifically developed to tackle the uniquely challenging and dynamic binary astrophysical scene presented by α Cen AB. The key results from our program are summarized below.

Table 2
Signal-to-noise Ratio Values and Empirical Significance (in Units of σ) of Different Exozodi Models and Geometries at Each Observation Epoch, alongside Zodi Levels for the Different Models

Geometry	ABA-1	ABA-2	ABA-3	ABA-4	"1-zodi"
			2025 February ($7.4 = 2.1\sigma$)[a]		
Coplanar	40.5 (11.6σ)	27.3 (7.9σ)	10.0 (2.9σ)	3.0 (0.9σ)	0.4 (0.1σ)
Offset	73.6 (21.2σ)	56.0 (16.1σ)	27.6 (7.9σ)	10.2 (2.9σ)	4.3 (1.2σ)
			2025 April ($5.0 = 1.3\sigma$)[a]		
Coplanar	78.7 (20.8σ)	52.6 (13.9σ)	21.3 (5.6σ)	5.8 (1.5σ)	-0.7 (-0.2σ)
Offset	86.1 (22.8σ)	46.8 (12.4σ)	14.8 (3.9σ)	4.4 (1.2σ)	0.6 (0.2σ)
Zodi Level					
Z_L[b]	58	17	5.1	1.8	0.94
Z_Σ[c]	84	29	8.4	3.0	1.0

Notes.
[a] Overall maximum S/N (and corresponding empirical significance) found in the original postprocessed data, with no model disk injected.
[b] The luminosity-based zodi level Z_L is defined as the ratio of the exozodi's fractional luminosity to that of the solar system's zodiacal cloud.
[c] The surface density-based zodi level Z_Σ is given by the ratio of the disk surface density at the Earth-equivalent insolation distance—approximately 1.23 au for α Cen A—to that of the solar system at 1 au.

Point-source sensitivity. We overcome extreme contamination from α Cen B and achieve a typical 5σ point-source contrast sensitivity between 10^{-5} and 10^{-4} for separations $\gtrsim 1''$, not only comparable to, but in some cases better than, those achieved for single star F1550C observations with JWST/MIRI. The improvements in contrast sensitivity are unique to α Cen A given its bright stellar magnitude, which yields a lower background limit in contrast space.

Exozodiacal disk sensitivity. While we did not detect any extended emission, injection–recovery tests with model exozodi disks show that our observations are sensitive to extended emission coplanar with α Cen AB, around α Cen A, at an unprecedented level of $\approx$5–8$\times$ the solar system's zodiacal cloud. This corresponds to the deepest limits on exozodi emission achieved for any stellar system to date and is a factor of $\sim$5–10 improvement over current state-of-the-art limits from nulling interferometry. The tremendous gain is a result of JWST's ability to resolve α Cen A's habitable zone (due to the star's proximity) and its excellent stability, which enables accurate subtraction of the stellar contribution.

Detection of planet candidate S1. A comprehensive search for point sources in the vicinity of α Cen A using both the classical median-RDI and joint PCA-KLIP subtraction strategies revealed one candidate, *S*1, $\approx 1\farcs5$ east of α Cen A, 3.5 mJy in brightness, and detected at an S/N between four and six in 2024 August. To investigate the nature of *S*1, we performed several tests, exploring the following possibilities.

1. *Is S1 a detector-level artifact in the α Cen AB integrations?* The independent detection of *S*1 in multiple subsets (first half, second half, even frames, odd frames, and individual integrations) of the α Cen AB data and the absence of any jumps in mean pixel brightness in an aperture centered on *S*1's location in the individual α Cen AB integrations shows that it is not likely a detector-level artifact (Section 4.2.3).
2. *Is S1 a PSF-subtraction artifact from α Cen B?* *S*1's signal persists both as the number of subsections in the annulus of joint PCA-KLIP reduction and the number of PCs used increase (Section 4.2.2). Importantly, *S*1 behaved distinctly than *A*1, a point-like source identified to be a residual PSF-subtraction artifact from α Cen B, in the above tests. *A*1 was not robust to changes in the reduction parameters. Additionally, the α Cen B PSF diffraction feature near the location of *S*1 in the 2024 August observation was also present in the 2025 February observation, but in the latter case, did not create a PSF-subtraction artifact in the reductions (Section 5.3). This is an independent argument that *S*1 is not likely a PSF-subtraction artifact from α Cen B.
3. *Is S1 an artifact from the ϵ Mus reference integrations?* The detection of *S*1 in all reductions performed by iteratively excluding frames from a single dither position ("leave-one-out" analysis, Section 4.2.4) shows that *S*1 is not likely an artifact from the on-axis ϵ Mus observations.
4. *Is S1 a background or foreground object?* Taking advantage of α Cen A's large proper motion ($\approx 3\farcs7$ yr^{-1}), we show that no point source is recovered at the location expected for *S*1 as a stationary background object in both the 2025 February and April observations (Section 5.1). The detection of *S*1 in the first and last integration of the $\approx$2.5 hr observing sequence, without any change in position, shows that *S*1 is not a high-proper motion foreground object (Section 4.2.3). Additionally, no sources are present at the location of α Cen A, during the 2024 August observations, according to the Minor Planet Catalog.
5. *Is S1 redetected as an orbiting planet in follow-up observations?* We did not recover *S*1 in a comprehensive search for point sources in the 2025 February and April observations. If *S*1 is astrophysical in nature (semimajor axis $\sim$ 1.5–2.5 au, orbital period $\sim$ 1.75–3.75 yr; Paper I), it is expected to exhibit significant orbital motion between 2024 August and the above epochs. In this scenario, *S*1 has moved to a region of poor sensitivity (e.g., within the coronagraph inner working angle or near the transition boundary), where it is undetectable. We generated 2D sensitivity maps for the 2025 February and April observations to enable constraints on the possible orbits of *S*1 consistent with a null detection in both epochs.

Together, the above results present a case for *S*1 as a planet, as opposed to an image artifact or contaminating astrophysical source, from a data reduction standpoint. An independent astrophysical case can be made for the plausibility of *S*1 as a planet and is the topic of Paper I. Because the August epoch had only one successful observation at a single roll angle, it is not possible to confirm that *S*1 is a bona fide planet. Nevertheless, *S*1 merits careful consideration as a candidate signal.

If astrophysical in nature, *S*1's nondetection in two follow-up observations (2025 February and April), conducted within 1 yr of candidate identification (2024 August), underscores the challenge of confirming short-period (∼few years) planets that exhibit significant (but, a priori, unknown) orbital motion, on the timescales of standard observing cycles, with direct imaging. Indeed, considering *S*1 together with VLT/NEAR candidate *C*1, Paper I shows that ∼50% of dynamically stable orbits, fit to the two astrometric points, would be consistent with nondetections in both follow-up observations. In such situations, several visits are needed to confirm planet candidates. Additional observations, with JWST or upcoming facilities (e.g., the Roman Coronagraph Instrument, the European Extremely Large Telescope, the Giant Magellan Telescope, or the TOLIMAN Space Telescope), are thus required to redetect candidate *S*1 before making the dramatic and exciting claim that a giant planet orbits our nearest Sun-like star. If *S*1 is confirmed as a new "α Cen Ab," it would be the nearest (1.33 pc), oldest (∼5 Gyr), coldest (≈225 K, Paper I), shortest period (≈2–3 yr, Paper I), and lowest-mass ($\lesssim$200 $M_{\oplus}$, Paper I) planet to be directly imaged around a solar-type star, to date. It would join a growing list of planets, with temperatures more comparable to our own Jupiter, to be directly imaged and amenable to follow-up spectroscopic observations: ϵ Ind Ab (E. C. Matthews et al. 2024), TWA 7b (K. A. Crotts et al. 2025; A.-M. Lagrange et al. 2025), 14 Her c (D. C. B. Gagliuffi et al. 2025), and the candidate/confirmed planets orbiting white dwarfs (M. A. Limbach et al. 2024, 2025; S. E. Mullally et al. 2024).

Acknowledgments

The STScI support staff provided invaluable assistance in the planning and execution of this program. In particular, we thank George Chapman and the Fine Guidance Sensor (FGS) team for their dedicated work in finding and vetting guide stars for this program and Wilson Joy Skipper and the short- and long-range planning teams for their contributions to this challenging observational program. The STScI's Director's office provided strong support for this program, from its initial selection as a high-risk, high-reward project, granting time to conduct test observations needed to validate the target acquisition strategy, to the execution of the follow-up DDT programs. We thank the referee for a prompt report and helpful comments that improved this manuscript.

This material is based upon work supported by the National Science Foundation Graduate Research Fellowship under Grant No. 2139433. Part of this work was carried out at the Jet Propulsion Laboratory, California Institute of Technology, under a contract with the National Aeronautics and Space Administration (80NM0018D0004). Programs PID#1618, #6797, and #9252 are supported through contracts JWST-GO-01618.001, JWST-GO-06797.001, and JWST-GO-09252.001. N.G. and E.C. acknowledge funding by the European Union (ERC, ESCAPE, project No. 101044152). Views and opinions expressed are however those of the author(s) only and do not necessarily reflect those of the European Union or the European Research Council Executive Agency. Neither the European Union nor the granting authority can be held responsible for them. All of the data presented in this Letter were obtained from the Mikulski Archive for Space Telescopes (MAST) at the Space Telescope Science Institute. The specific observations analyzed can be accessed via doi: 10.17909/v8nv-vx17 for the 2024 August observations, doi: 10.17909/cb0x-rn85 for the 2025 February observations, and doi: 10.17909/3z9q-9f65 for the 2025 April observations. STScI is operated by the Association of Universities for Research in Astronomy, Inc., under NASA contract NAS5-26555. Support to MAST for these data is provided by the NASA Office of Space Science via grant NAG5-7584 and by other grants and contracts. This research has made use of NASA's Astrophysics Data System. Software citation information were aggregated using `The Software Citation Station` [30] (T. Wagg & F. S. Broekgaarden 2024; T. Wagg et al. 2024).

Author Contributions

A.S. led the writing and submission of this manuscript under the guidance of C.B. and D.M. W.B. conducted the JWST pipeline processing of the MIRI observations. A.S. led the postprocessing analysis of the MIRI observations for point sources and extended emission. N.G., M.S., M.W., and E.C. performed the S/N calculations for extended emission. L.P., A.B., and J.L.-S. conducted independent postprocessing of the MIRI observations to validate the results. K.W., A.B., and P.O. L. provided advice on data reduction. Dust emission models for the exozodiacal disk were developed by M.S. and M.W. P. K. provided the ephemeris for α Cen A. All authors discussed the results and commented on the manuscript.

Facility: JWST (MIRI).

Software: `astropy` (Astropy Collaboration et al. 2013, 2018, 2022), `matplotlib` (J. D. Hunter 2007), `numpy` (C. R. Harris et al. 2020), `pandas` (W. McKinney 2010; The pandas development team 2025), `Python` (G. Van Rossum & F. L. Drake 2009), `scipy` (P. Virtanen et al. 2020; R. Gommers et al. 2023), `astroquery` (A. Ginsburg et al. 2019, 2024), `scikit-image` (S. van der Walt et al. 2014), `STPSF` (M. D. Perrin et al. 2012; M. D. Perrin et al. 2014), `jwst` (H. Bushouse et al. 2025), `pyKLIP` (J. J. Wang et al. 2015), `vip` (C. A. Gomez Gonzalez et al. 2017; V. Christiaens et al. 2023), `spaceKLIP` (J. Kammerer et al. 2022; A. L. Carter et al. 2023; A. Carter et al. 2025), and `webbpsf_ext` (J. Leisenring 2025).

Appendix A
To Bin or Not to Bin: Example Comparison with the 2025 February Observations

For each observation epoch, we obtained 400 integrations per dither position in the ϵ Mus on-axis observations and 1250 integrations per ϵ Mus off-axis observation. An interesting question to investigate is whether we should median combine (bin) all integrations of a given ϵ Mus (on-/off-axis) reference observation before PSF subtraction. The primary reason to retain all integrations as part of the reference library would be to leverage the frame-to-frame PSF diversity to improve PSF subtraction with PCA-KLIP. Here, we test the above through

[30] https://www.tomwagg.com/software-citation-station/

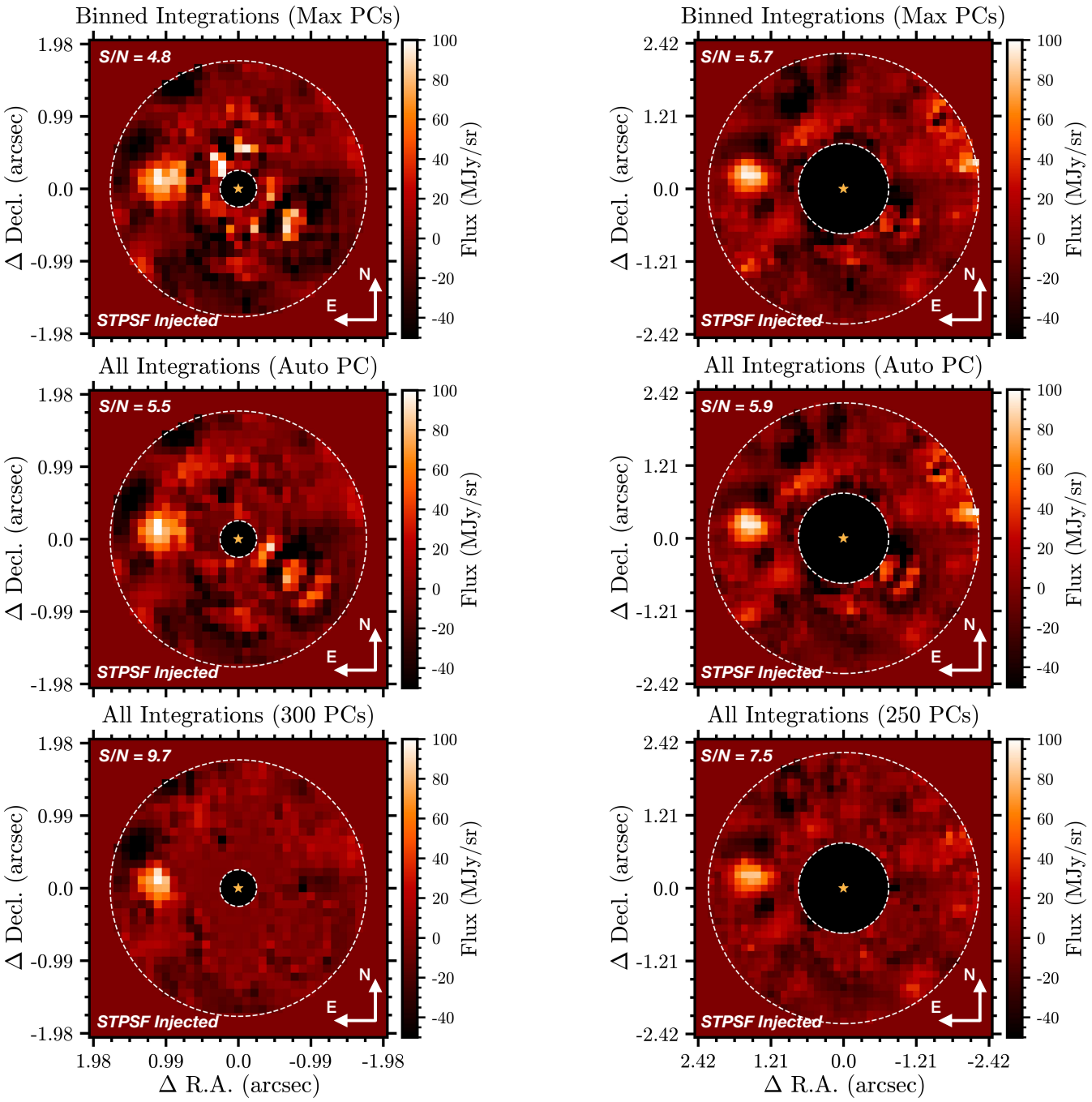

Figure A1. Left column: reduced images showing the recovery of a synthetic STPSF model injected at a separation of 1″ and a PA of 80° in the 2025 February observations. From top to bottom are reductions with a binned reference library, a reference library with all the integrations used and the number of PCs automatically selected, and a reference library with all the integrations used and the number of PCs selected to maximize the S/N of the injected companion, respectively. Right column: same as the left column for injections at a separation of 1.″5. Using all the integrations results in a higher S/N recovery of the injected source compared to binning the integrations.

an example PSF injection–recovery test conducted with the 2025 February observations. We inject a 3 mJy STPSF model at separations of 1″ and 1.″5 at a PA of 80° in the raw α Cen AB cube. Three types of reductions are performed with PCA-KLIP applied to a three FWHM diameter annular region centered on the injected source's location: (1) all the off-axis and each dither position of the on-axis ϵ Mus reference integrations are binned (mean stacked) to a single frame (total number of reference frames after binning = 1 off axis + 9 on axis + 9 on axis) and the number of PCs is manually chosen to maximize the injected companion S/N; (2) all ϵ Mus reference integrations are used without binning (total number of reference frames = 1250 off axis + 9 × 400 on axis + 9 × 400 on axis) and the number of PCs is automatically chosen as described in Section 4.2.1; and (3) all ϵ Mus reference integrations are used without binning and the number of PCs is manually chosen to maximize the injected companion S/N. In the third case, we noticed that at very many PC

(approaching the maximum) artifacts are created at the pixel level, which artificially inflate the estimated S/N, even though the reduced images show that the synthetic companion has been severely oversubtracted. Thus, the reduced images had to be visually inspected to reliably select the optimal number of PCs. This issue makes it impractical to manually tune the number of PCs in our full set of injection–recovery tests to generate 2D sensitivity maps (Section 7).

For both injection separations, we find that using all the integrations without binning recovers the synthetic companion at a higher S/N as compared to the reductions where the reference integrations were binned (Figure A1; 19 PCs, the maximum possible, was preferred for the binned reductions). Further, we find that manually tuning the number of PCs can further improve confidence in the detectability of a point source, compared to auto-PC selection (Figure A1), as was also seen in the analysis presented in Section 4.2.2 for the 2024 August observations. While the results of the comparison are only presented for two injection locations (to serve as examples), we find that the same conclusions generally hold true at other separations and PAs of injection as well. Given these results, we chose not to bin the individual reference integrations before PSF subtraction.

The temporal behavior of wavefront variations of JWST have been reported in detail by R. C. Telfer et al. (2024). At the timescale of our single integrations, ∼7.5 s, shorter vibrations dominate at the ∼200 pm level. At the timescale of minutes, ISIM Electronics Compartment (IEC) oscillations dominate with wavefront variations of the order of ∼1 nm. The effect of the IEC oscillations can be seen in the power spectrum of the PCs computed from the set of science or reference integrations. This explains why using a single integration PSF library performs better. The above analysis will be discussed in more detail in future work.

Appendix B
Recovery of Known Background Sources

P. Kervella et al. (2016) presented a catalog of the expected close conjunctions between the α Cen AB system and stars in the background. Among them, sources S2 and S5 (hereafter referred to as KS2 and KS5) are expected to be in the vicinity of α Cen A during the time of our observations. Indeed, KS5 is seen in the α Cen AB integration even before PSF subtraction at the edge of the detector (Figure 1). This is the bright source that α Cen A is rapidly moving toward in upcoming years with a distance of closest approach $\rho_{\rm min} = 0\farcs015 \pm 0\farcs135$ in ∼2028 (P. Kervella et al. 2016). KS2 is expected to be located ≈6.″3, ≈6.″9, and ≈8.″3 east from α Cen A for the 2024 August, 2025 February, and 2025 April observing dates, respectively, and has a low F1550C flux of ∼1 mJy. We use this source as a test object to check if PCA-KLIP can recover it. We performed joint PCA-KLIP in an annulus with a width of three FWHM divided into eight subsections, centered at the radial separation expected for KS2 in each epoch, and with the number of PCs automatically selected as discussed in Section 4.2.1. KS2 is clearly detected at the expected location in each epoch (Figure B1). For the April data set specifically, KS2 is only detected in the roll 1 observation as it lies along the 4QPM transition boundary for the second roll.

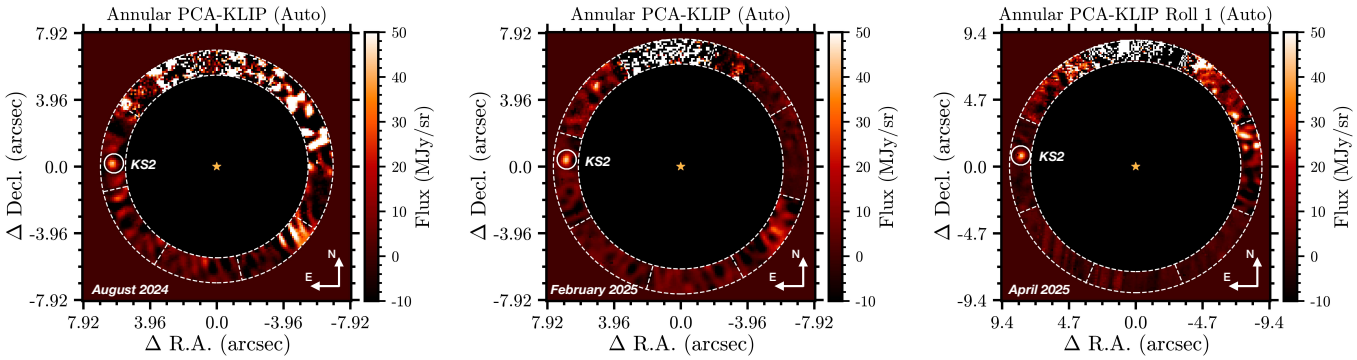

Figure B1. From left to right, joint PCA-KLIP-reduced images for the 2024 August, 2025 February, and 2025 April (roll 1) epoch observations showing the detection of the ∼1 mJy background source KS2 (circled) from P. Kervella et al. (2016).

ORCID iDs

Aniket Sanghi https://orcid.org/0000-0002-1838-4757
Charles Beichman https://orcid.org/0000-0002-5627-5471
Dimitri Mawet https://orcid.org/0000-0002-8895-4735
William O. Balmer https://orcid.org/0000-0001-6396-8439
Nicolas Godoy https://orcid.org/0000-0003-0958-2150
Laurent Pueyo https://orcid.org/0000-0003-3818-408X
Anthony Boccaletti https://orcid.org/0000-0001-9353-2724
Max Sommer https://orcid.org/0000-0003-4761-5785
Alexis Bidot https://orcid.org/0000-0002-9799-2303
Elodie Choquet https://orcid.org/0000-0002-9173-0740
Pierre Kervella https://orcid.org/0000-0003-0626-1749
Jarron Leisenring https://orcid.org/0000-0002-0834-6140
Jorge Llop-Sayson https://orcid.org/0000-0002-3414-784X
Michael Ressler https://orcid.org/0000-0001-5644-8830
Kevin Wagner https://orcid.org/0000-0002-4309-6343
Mark Wyatt https://orcid.org/0000-0001-9064-5598

References

Akeson, R., Beichman, C., Kervella, P., Fomalont, E., & Benedict, G. F. 2021, AJ, 162, 14
Apai, D., Kasper, M., Skemer, A., et al. 2016, ApJ, 820, 40
Astropy Collaboration, Price-Whelan, A. M., Lim, P. L., et al. 2022, ApJ, 935, 167
Astropy Collaboration, Price-Whelan, A. M., Sipőcz, B. M., et al. 2018, AJ, 156, 123
Astropy Collaboration, Robitaille, T. P., Tollerud, E. J., et al. 2013, A&A, 558, A33
Beichman, C., Ygouf, M., Llop Sayson, J., et al. 2020, PASP, 132, 015002
Beichman, C., Sanghi, A., Mawet, D., et al. 2025, ApJL, 989, L22
Boccaletti, A., Cossou, C., Baudoz, P., et al. 2022, A&A, 667, A165
Boccaletti, A., Lagage, P.-O., Baudoz, P., et al. 2015, PASP, 127, 633
Brandt, T. D. 2024, PASP, 136, 045004
Bushouse, H., Eisenhamer, J., Dencheva, N., et al. 2025, JWST Calibration Pipeline, v1.18.0, Zenodo, doi:10.5281/zenodo.15178003
Carter, A., Kammerer, J., Leisenring, J., et al. 2025, spaceKLIP: JWST coronagraphy data data reduction and analysis pipeline, Astrophysics Source Code Library, ascl:2502.014
Carter, A. L., Hinkley, S., Kammerer, J., et al. 2023, ApJL, 951, L20
Christiaens, V., Gonzalez, C., Farkas, R., et al. 2023, JOSS, 8, 4774
Crotts, K. A., Carter, A. L., Lawson, K., et al. 2025, ApJ, 987, 41
Ertel, S., Defrère, D., Hinz, P., et al. 2018, AJ, 155, 194
Ertel, S., Defrère, D., Hinz, P., et al. 2020, AJ, 159, 177
Gagliuffi, D. C. B., Balmer, W. O., Pueyo, L., et al. 2025, ApJ, 988, 18
Ginsburg, A., Sipöcz, B., Brasseur, C. E., et al. 2024, astropy/astroquery: v0.4.7, Zenodo, doi:10.5281/zenodo.10799414
Ginsburg, A., Sipőcz, B. M., Brasseur, C. E., et al. 2019, AJ, 157, 98
Gomez Gonzalez, C. A., Wertz, O., Absil, O., et al. 2017, AJ, 154, 7
Gommers, R., Virtanen, P., Burovski, E., et al. 2023, scipy/scipy: SciPy v1.11.2, Zenodo, doi:10.5281/zenodo.8259693
Greenbaum, A. Z., Llop-Sayson, J., Lew, B. W., et al. 2023, ApJ, 945, 126
Harris, C. R., Millman, K. J., Walt, S. J. v. d., et al. 2020, Natur, 585, 357
Hunter, J. D. 2007, CSE, 9, 90
Joyce, M., & Chaboyer, B. 2018, ApJ, 864, 99
Kammerer, J., Girard, J., Carter, A. L., et al. 2022, Proc. SPIE, 12180, 1369
Kelsall, T., Weiland, J. L., Franz, B. A., et al. 1998, ApJ, 508, 44
Kervella, P., Mignard, F., Mérand, A., & Thévenin, F. 2016, A&A, 594, A107
Lafrenière, D., Marois, C., Doyon, R., & Barman, T. 2009, ApJ, 694, L148
Lafreniere, D., Marois, C., Doyon, R., Nadeau, D., & Artigau, E. 2007, ApJ, 660, 770
Lagrange, A. M., Bonnefoy, M., Chauvin, G., et al. 2010, Sci, 329, 57
Lagrange, A.-M., Wilkinson, C., Mâlin, M., et al. 2025, Natur, 642, 905
Leisenring, J. 2025, WebbPSF Extensions, v2.0.1, Zenodo, doi:10.5281/zenodo.15086592
Limbach, M. A., Vanderburg, A., MacDonald, R. J., et al. 2025, ApJL, 984, L28
Limbach, M. A., Vanderburg, A., Venner, A., et al. 2024, ApJL, 973, L11
Liu, M. C. 2004, Sci, 305, 1442
Marois, C., Lafrenière, D., Doyon, R., Macintosh, B., & Nadeau, D. 2006, ApJ, 641, 556
Marois, C., Macintosh, B., & Véran, J.-P. 2010, Proc. SPIE, 7736, 77361J
Matthews, E. C., Carter, A. L., Pathak, P., et al. 2024, Natur, 633, 789
Mawet, D., Milli, J., Wahhaj, Z., et al. 2014, ApJ, 792, 97
McKinney, W. 2010, in Proc. 9th Python in Science Conf., ed. S. van der Walt & J. Millman, 56
Mullally, S. E., Debes, J., Cracraft, M., et al. 2024, ApJL, 962, L32
Mâlin, M., Boccaletti, A., Perrot, C., et al. 2024, A&A, 690, A316
Mâlin, M., Boccaletti, A., Perrot, C., et al. 2025, A&A, 693, 315
Perrin, M. D., Sivaramakrishnan, A., Lajoie, C.-P., et al. 2014, Proc. SPIE, 9143, 91433X
Perrin, M. D., Soummer, R., Elliott, E. M., Lallo, M. D., & Sivaramakrishnan, A. 2012, Proc. SPIE, 8442, 84423D
Pueyo, L. 2016, ApJ, 824, 117
Quarles, B., & Lissauer, J. J. 2016, AJ, 151, 111
Rigby, J., Perrin, M., McElwain, M., et al. 2023, PASP, 135, 048001
Rigley, J. K., & Wyatt, M. C. 2020, MNRAS, 497, 1143
Sanghi, A., Beichman, C., Mawet, D., et al. 2025, RNAAS, 9, 119
Sanghi, A., Zhou, Y., & Bowler, B. P. 2022, AJ, 163, 119
Schroeder, D. J., & Golimowski, D. A. 1996, PASP, 108, 510
Schroeder, D. J., Golimowski, D. A., Brukardt, R. A., et al. 2000, AJ, 119, 906
Sommer, M., Wyatt, M., & Han, Y. 2025, MNRAS, 539, 439
Soummer, R., Pueyo, L., & Larkin, J. 2012, ApJ, 755, L28
The pandas development team 2025, pandas-dev/pandas: Pandas, v2.3.0, Zenodo, doi: 10.5281/zenodo.15597513
Telfer, R. C., Meléndez, M., Flagey, N., et al. 2024, Proc. SPIE, 13092, 306
Thévenin, F., Provost, J., Morel, P., et al. 2002, A&A, 392, L9
Turnbull, M. C. 2015, arXiv:1510.01731
van der Walt, S., Schönberger, J. L., Nunez-Iglesias, J., et al. 2014, PeerJ, 2, e453
Van Rossum, G., & Drake, F. L. 2009, Python 3 Reference Manual (Scotts Valley, CA: CreateSpace)
Virtanen, P., Gommers, R., Oliphant, T. E., et al. 2020, NatMe, 17, 261
Wagg, T., Broekgaarden, F., & Gültekin, K. 2024, TomWagg/software-citation-station: v1.2, Zenodo, doi: 10.5281/zenodo.13225824
Wagg, T., & Broekgaarden, F. S. 2024, arXiv:2406.04405
Wagner, K., Boehle, A., Pathak, P., et al. 2021, NatCo, 12, 922
Wang, J. J., Graham, J. R., Pueyo, L., et al. 2016, AJ, 152, 97
Wang, J. J., Ruffio, J.-B., De Rosa, R. J., et al. 2015, pyKLIP: PSF Subtraction for Exoplanets and Disks, Astrophysics Source Code Library, ascl:1506.001
Wiegert, P. A., & Holman, M. J. 1997, AJ, 113, 1445
Wright, G. S., Wright, D., Goodson, G. B., et al. 2015, PASP, 127, 595
Zhao, L., Fischer, D. A., Brewer, J., Giguere, M., & Rojas-Ayala, B. 2018, AJ, 155, 24
Zhou, Y., Bowler, B. P., Wagner, K. R., et al. 2021, AJ, 161, 244